Advancing LHC probes of dark matter from the inert two-Higgs-doublet model with the monojet signal

A. Belyaev and S. Moretti

Particle Physics Department, Rutherford Appleton Laboratory,
Chilton, Didcot, Oxon OX11 0QX, United Kingdom
and School of Physics and Astronomy, University of Southampton,
Southampton SO17 1BJ, United Kingdom

T. R. Fernandez Perez Tomei and S. F. Novaes

Universidade Estadual Paulista, R. Dr. Bento Teobaldo Ferraz, 271—Várzea da Barra Funda,
São Paulo, São Paulo 01140-070 Brazil

P. G. Mercadante

Universidade Federal do ABC, Avenida dos Estados, 5001, Bangú
Santo Andre, Sao Paulo 09210-580. Brazil

C. S. Moon

Kyungpook National University, Daegu 41566, Korea

L. Panizzi

Department of Physics and Astronomy, Uppsala University, Box 516, SE-751 20 Uppsala, Sweden
and School of Physics and Astronomy, University of Southampton, Southampton SO17 1BJ, United Kingdom

F. Rojas

Universidad Técnica Federico Santa María, Avenida España 1680, Valparaíso, Chile
and School of Physics and Astronomy, University of Southampton, Southampton SO17 1BJ, United Kingdom

M. Thomas

School of Physics and Astronomy, University of Southampton, Southampton SO17 1BJ, United Kingdom

The inert two-Higgs-doublet Model (i2HDM) is a well-motivated minimal consistent dark matter (DM) model, but it is rather challenging to test at the LHC in the parameter space allowed by relic density and DM direct detection constraints. This is especially true when considering the latest XENON 1T data on direct DM searches, which we use here to present the best current combined limit on the i2HDM parameter space. In this analysis, we present prospects to advance the exploitation of DM monojet signatures from the i2HDM at the LHC, by emphasising that a shape analysis of the missing transverse momentum distribution allows one to sizably improve the LHC discovery potential. For a key element of our analysis, we explore the validity of using an effective vertex, ggH, for the coupling of the Higgs boson to gluons using a full one-loop computation. We have found sizeable differences between the two approaches, especially in the high missing transverse momentum region, and incorporated the respective K-factors to obtain the correct kinematical distributions. As a result, we delineate a realistic search strategy and present the improved current and projected LHC sensitivity to the i2HDM parameter space.

I. INTRODUCTION

Despite several independent evidences of dark matter (DM) at the cosmological scale, its nature remains unknown since no experiment so far has been able to claim its detection in the laboratory and probe its

properties. Potentially, DM can be probed in direct or indirect detection experiments as well as be produced at the LHC or future machines, though the latter can only detect DM *candidates*, as any observed missing energy can still be interpreted as generated by long-lived neutral particles. This combined effort on advancing our knowledge of DM properties is one of the key goals of the astroparticle and high energy physics communities.

A convenient way to understand the potential of both collider and noncollider experiments to probe DM is to explore simple, fully calculable, renormalizable models with viable DM candidates, which we refer to as minimal consistent dark matter (MCDM) models. We do not know yet which theoretical scenario corresponds to reality, but any model of this kind offers an excellent opportunity to gain insight into the intricate interplay between collider and noncollider constraints. MCDM models, which can be viewed as robust toy models, are self-consistent and can be easily incorporated into larger theoretically driven scenarios of physics beyond the Standard Model. Because of their attractive features, MCDM models can be considered as the next step beyond DM effective field theory (EFT) (see e.g. Refs. [1–13]) and simplified DM models (see e.g. Refs. [14–21]).

The inert two-Higgs-doublet model (i2HDM), which was initially suggested more than 30 years ago in Ref. [22], is one of the most representative MCDM models which has become very attractive lately [23–45] in the light of intensive DM searches. In fact, besides providing a good DM candidate, the i2HDM can also give rise to an "improved naturalness" [24] since large radiative corrections from the inert Higgs sector can screen the SM Higgs contribution to the eletroweak (EW) parameter ΔT.

It was shown in Ref. [45] that the LHC has limited sensitivity to probe the i2HDM with the monojet signature using the cut-based analyses optimized for the low-luminosity Run 2 data. To complement these studies, in the present paper, we explore the LHC potential to probe DM via the monojet signature in the i2HDM scenario by exploiting a larger amount of information from observables at the differential level. More specifically, we will consider the shape of the missing transverse momentum (E_T^{miss}) distribution. New findings of this study include a) updating limits on the i2HDM parameter space following the recent XENON 1T results on DM direct detection (DD) searches; b) exploring the range of validity of the effective ggH vertex in the heavy top mass limit by considering the E_T^{miss} distribution and comparing its shape to the full one-loop result, which will allow us to determine a realistic LHC potential for probing DM in different kinematical regions; c) optimizing and improving the LHC sensitivity to the DM monojet signal from the i2HDM defined by Higgs and Z-boson mediation processes using a shape analysis of the E_T^{miss} distribution; d) projecting our results to the High Luminosity LHC (HL-LHC) phase.

The rest of the paper is organized as follows. In Sec. II, we discuss the i2HDM parameter space together with the current status of theoretical and experimental constraints. In Sec. III, we present the main results of the paper, which include the analysis of the validity of the effective ggH (H being the SM-like Higgs) vertex approach, the exploration of several model benchmarks, and finally finding the LHC potential to probe the i2HDM at present and projected luminosities via exploitation of the E_T^{miss} shape in the monojet signature. In Sec. IV, we draw our conclusions.

II. I2HDM

A. Parameter space

The i2HDM [22–25] is an extension of the Standard Model (SM) with a second scalar doublet ϕ_2 possessing the same quantum numbers as the SM Higgs doublet ϕ_1 but with no couplings to fermions, thus providing its inert nature. This construction is protected by a discrete $\mathcal{Z}_2$ symmetry under which ϕ_2 is odd and all the other fields are even. The Lagrangian of the scalar sector is

$$\mathcal{L} = |D_\mu \phi_1|^2 + |D_\mu \phi_2|^2 - V(\phi_1, \phi_2), \quad (1)$$

where V is the potential with all scalar interactions compatible with the $\mathcal{Z}_2$ symmetry:

$$\begin{aligned} V = & -m_1^2(\phi_1^\dagger \phi_1) - m_2^2(\phi_2^\dagger \phi_2) + \lambda_1(\phi_1^\dagger \phi_1)^2 + \lambda_2(\phi_2^\dagger \phi_2)^2 \\ & + \lambda_3(\phi_1^\dagger \phi_1)(\phi_2^\dagger \phi_2) + \lambda_4(\phi_2^\dagger \phi_1)(\phi_1^\dagger \phi_2) \\ & + \frac{\lambda_5}{2}[(\phi_1^\dagger \phi_2)^2 + (\phi_2^\dagger \phi_1)^2]. \end{aligned} \quad (2)$$

In the unitary gauge, the doublets take the form

$$\phi_1 = \frac{1}{\sqrt{2}} \begin{pmatrix} 0 \\ v + H \end{pmatrix}, \qquad \phi_2 = \frac{1}{\sqrt{2}} \begin{pmatrix} \sqrt{2}h^+ \\ h_1 + ih_2 \end{pmatrix}, \quad (3)$$

where we consider the parameter space in which only the first, SM-like doublet acquires a vacuum expectation value, v. In the notation $\langle \phi_i^0 \rangle = v_i/\sqrt{2}$, this inert minimum corresponds to $v_1 = v$, $v_2 = 0$. After EW symmetry breaking, the $\mathcal{Z}_2$ symmetry is still conserved by the vacuum state, which forbids direct coupling of any single inert field to the SM fields and protects the lightest inert boson from decaying, hence providing the DM candidate in this scenario. In contrast, the interactions of a *pair* of inert scalars with the SM gauge bosons and SM-like Higgs H are allowed, thus giving rise to various signatures at colliders and at DM detection experiments.

In addition to the SM-like scalar H, the model contains one inert charged $h^\pm$ and two further inert neutral h_1, h_2 scalars. The two neutral scalars of the i2HDM have

opposite CP parities, but it is impossible to unambiguously determine which of them is CP even and which one is CP odd since the model has two CP symmetries, $h_1 \rightarrow h_1$, $h_2 \rightarrow -h_2$ and $h_1 \rightarrow -h_1$, $h_2 \rightarrow h_2$, which get interchanged upon a change of basis $\phi_2 \rightarrow i\phi_2$. This makes the specification of the CP properties of h_1 and h_2 a basis-dependent statement. Therefore, following Ref. [45], we denote the two neutral inert scalar masses as $M_{h_1} < M_{h_2}$, without specifying which is scalar or pseudoscalar, so that h_1 is the DM candidate.

The model can be conveniently described by a five-dimensional parameter space [45] using the following phenomenologically relevant variables,

$$M_{h_1}, \qquad M_{h_2} > M_{h_1}, \qquad M_{h^+} > M_{h_1}, \qquad \lambda_2 > 0,$$
$$\lambda_{345} > -2\sqrt{\lambda_1 \lambda_2}, \tag{4}$$

where M_{h_1}, M_{h_2}, and M_{h^+} are the masses of the two neutral and charged inert scalars, respectively, whereas

$\lambda_{345} = \lambda_3 + \lambda_4 + \lambda_5$ is the coupling which governs the Higgs-DM interaction vertex Hh_1h_1. The masses of the physical scalars are expressed in terms of the parameters of the Lagrangian in Eqs. (1) and (2) as follows:

$$M_H^2 = 2\lambda_1 v^2 = 2m_1^2,$$
$$M_{h^+}^2 = \frac{1}{2}\lambda_3 v^2 - m_2^2,$$
$$M_{h_1}^2 = \frac{1}{2}(\lambda_3 + \lambda_4 - |\lambda_5|)v^2 - m_2^2,$$
$$M_{h_2}^2 = \frac{1}{2}(\lambda_3 + \lambda_4 + |\lambda_5|)v^2 - m_2^2 > M_{h_1}^2. \tag{5}$$

B. Theoretical and experimental constraints

Constraints on the Higgs potential from requiring vacuum stability and a global minimum take the following form [45],

$$\begin{cases} M_{h_1}^2 > 0 \text{ (the trivial one)} & \text{for } |R| < 1, \\ M_{h_1}^2 > (\lambda_{345}/2\sqrt{\lambda_1 \lambda_2} - 1)\sqrt{\lambda_1 \lambda_2}v^2 = (R-1)\sqrt{\lambda_1 \lambda_2}v^2 & \text{for } R > 1, \end{cases} \tag{6}$$

where $R = \lambda_{345}/2\sqrt{\lambda_1 \lambda_2}$ and $\lambda_1 \approx 0.129$ is fixed as in the SM by the Higgs mass in Eq. (5). The latter condition places an important upper bound on λ_{345} for a given DM mass M_{h_1}.

The theoretical upper limit on λ_{345} for a given DM mass comes from the vacuum stability constraint. Using Eq. (17) from Ref. [45] and an upper limit on λ_2 (which is about $4\pi/3$ for DM masses below 300 GeV), we find

$$\lambda_{345} < 2\left(\frac{M_{h_1}^2}{v^2} + \sqrt{\lambda_1 \lambda_2^{\max}}\right) \simeq 2\left(\frac{M_{h_1}^2}{v^2} + \sqrt{\lambda_1 \frac{4\pi}{3}}\right). \tag{7}$$

When $M_{h_1} < M_H/2$, λ_{345} has a much stronger limit coming from the invisible Higgs boson decay measured at the LHC. In this region, the limit on $|\lambda_{345}|$ can be written in the following form,

$$|\lambda_{345}| < \left(\frac{8\pi g_W^2 \Gamma_{SM} M_H}{M_W^2 (\frac{1}{Br(H\rightarrow invis)} - 1)\sqrt{1 - 4\frac{M_{h_1}^2}{M_H^2}}}\right)^{1/2}, \tag{8}$$

where $Br(H \rightarrow invis)$ is the experimental limit on the branching ratio (Br) for invisible Higgs boson decays, Γ_{SM} is the SM-like Higgs boson width, and g_W is the SM weak coupling. This formula is derived under the assumption that $H \rightarrow h_1h_1$ is the only invisible channel of the SM-like Higgs boson. In Fig. 1, we present values of

$|\lambda_{345}|_{\max}$ as a function of M_{h_1} for several values of $Br(H \rightarrow invis)$ including 0.25 and 0.24 corresponding to the most up-to-date limits on $Br(H \rightarrow invis)$ from ATLAS [46] and CMS [47], respectively. One should note that experimental limits on $Br(H \rightarrow invis)$ are actually placed for $H \rightarrow invis$ to *any channel* and thus also include $H \rightarrow ZZ \rightarrow$ neutrinos, which is, however, below the per mille level and can thus be neglected in our study.

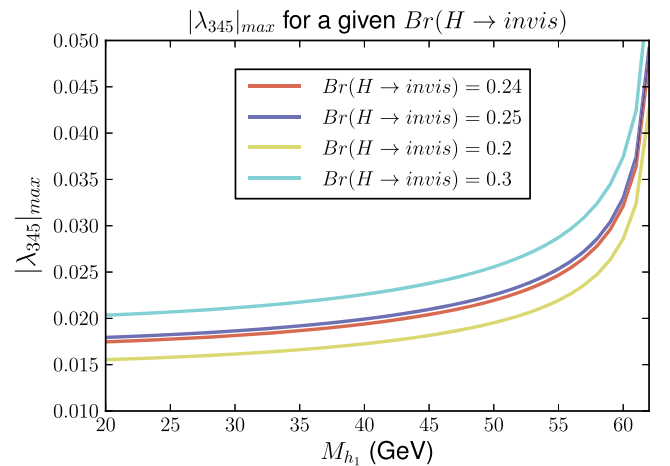FIG. 1. The values of $|\lambda_{345}|_{\max}$ as a function of M_{h_1} for selected choices of $Br(H \rightarrow invis)$. This limit is found under the assumption that $H \rightarrow h_1h_1$ is the only invisible decay channel of the SM-like Higgs boson.
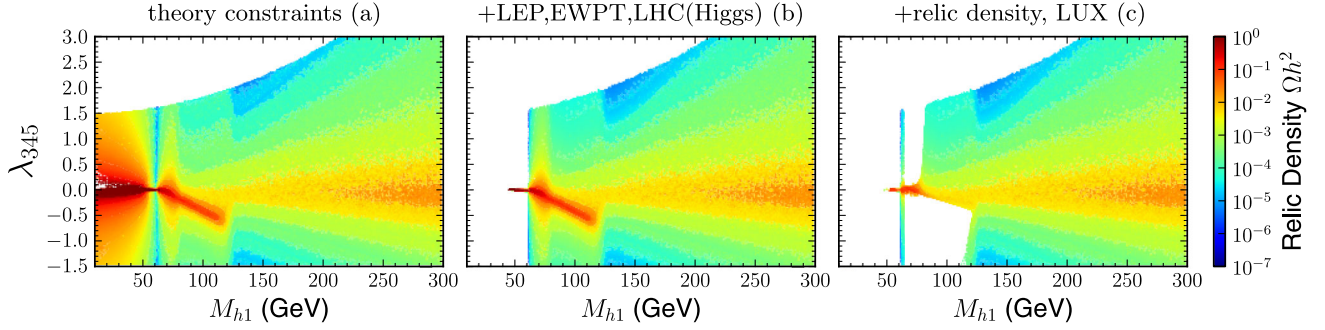
FIG. 2. Color maps of DM relic abundance projected on the plane (M_{h_1}, λ_{345}) from Ref. [45]. The three plots correspond to the surviving points after the sequential application of the sets of constraints described in the text.

The $|\lambda_{345}|_{\max}$ value increases when M_{h_1} approaches $M_H/2$, ranging from 0.024 at $M_{h_1} = 50$ GeV to 0.053 at $M_{h_1} = 62$ GeV. At the same time, the $\Omega h^2 < 0.1$ constraint sets the lower limit $M_{h_1} \gtrsim 40$ GeV since below it there are no effective annihilation and/or co-annihilation DM channels to bring DM relic density to a low enough level consistent with Planck constraints. One should note that when the decay $H \to h_2 h_2$ also takes place and when h_1 and h_2 are close in mass (below, say a few giga-electron-volts) this channel will also contribute to the invisible Higgs decay. In this case, the limit on λ_{345} can be easily modified, taking into account that $\lambda_{Hh_2h_2} = \lambda_{345} + \frac{M_{h_2}^2 - M_{h_1}^2}{v^2}$, and thus for $M_{h_2} \simeq M_{h_1}$, one has $\lambda_{Hh_2h_2} \simeq \lambda_{Hh_1h_1} = \lambda_{345}$.

The comprehensive analysis of the i2HDM parameter space performed in Ref. [45] using an i2HDM implementation into the CALCHEP [48] and MICROMEGAS [49,50] frameworks demonstrates an important complementarity of various constraints, which is presented in Fig. 2 as an effect of the sequential application of a) theoretical constraints from vacuum stability, perturbativity, and unitarity (theory); b) experimental constraints from colliders [Large Electron–Positron collider (LEP) and LHC Higgs data, including those from EW precision test (EWPT) data]; and c) the upper bound on the DM relic density at $\Omega_{\text{DM}} h^2$ given by Planck [51,52] and constraints from DM DD searches at LUX [53].

From Figs. 2(a) and 2(b), one can see the large effect of the invisible Higgs decay constraint on λ_{345} (of the order of 10^{-2}) in the $M_{h_1} < M_H/2$ region, which is 2 orders of magnitude stronger than the constraint on λ_{345} from vacuum stability. The constraint from DM DD searches from LUX [53] further limits λ_{345} as one can see from Fig. 2(c). Let us recall first that we use the rescaled DD spin-independent (SI) cross section, $\hat{\sigma}_{\text{SI}} = R_\Omega \times \sigma_{\text{SI}}$, where the scaling factor $R_\Omega = \Omega_{\text{DM}}/\Omega_{\text{DM}}^{\text{Planck}}$ takes into account the case of h_1 representing only a part of the total DM budget, thus allowing for a convenient comparison of the model predictions with the DM DD limits. One can see that this constraint is not symmetric with respect to the sign of λ_{345}; the parameter space with $\lambda_{345} < 0$ receives stronger
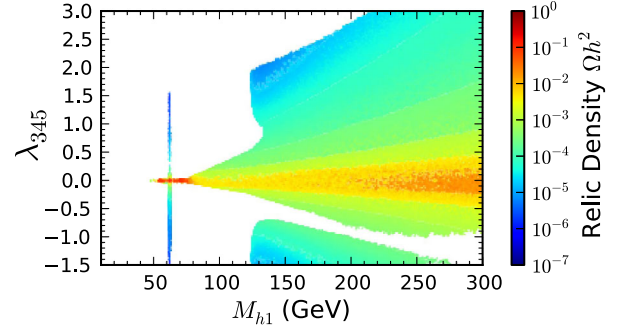

FIG. 3. The new constraints on the i2HDM parameter space from XENON1T searches for DM [54].

constraints. The reason for this is that the sign of λ_{345} defines the sign of the interference of DM annihilation into EW gauge bosons via the Higgs boson and via the $h_1 h_1 VV$ quartic coupling. For positive λ_{345}, the interference is positive, and the relic density is correspondingly lower, so the DM DD rates rescaled with relic density, $\hat{\sigma}_{\text{SI}}$, are lower than for the case of negative λ_{345}, when the corresponding interference is negative and the relic density is higher. One should also note that the combined constraints exclude $M_{h_1} < 45$ GeV for the whole parameter space of the i2HDM.

Since DM DD constraints play an important role, in the light of recent results from the XENON1T experiment [54], we have performed a further comprehensive scan of the i2HDM parameter space analogously to Ref. [45] and have found new constraints.[1] Our results are shown in Fig. 3, where we present the i2HDM parameter space left after the application of theory, LEP, EWPT, LHC constraints as well as upper bounds on the relic density from Planck and DM DD limits from XENON1T. One can see a large effect of the XENON1T constraints on λ_{345}, which improve LUX limits by more than 1 order of magnitude, chiefly, over the $M_H/2 < M_{h_1} < 125$ GeV region. In particular, in this region, $|\lambda_{345}|$ is limited to be always

---

[1]For the XENON1T limit, we have used digitized data from the PHENODATA database [55].
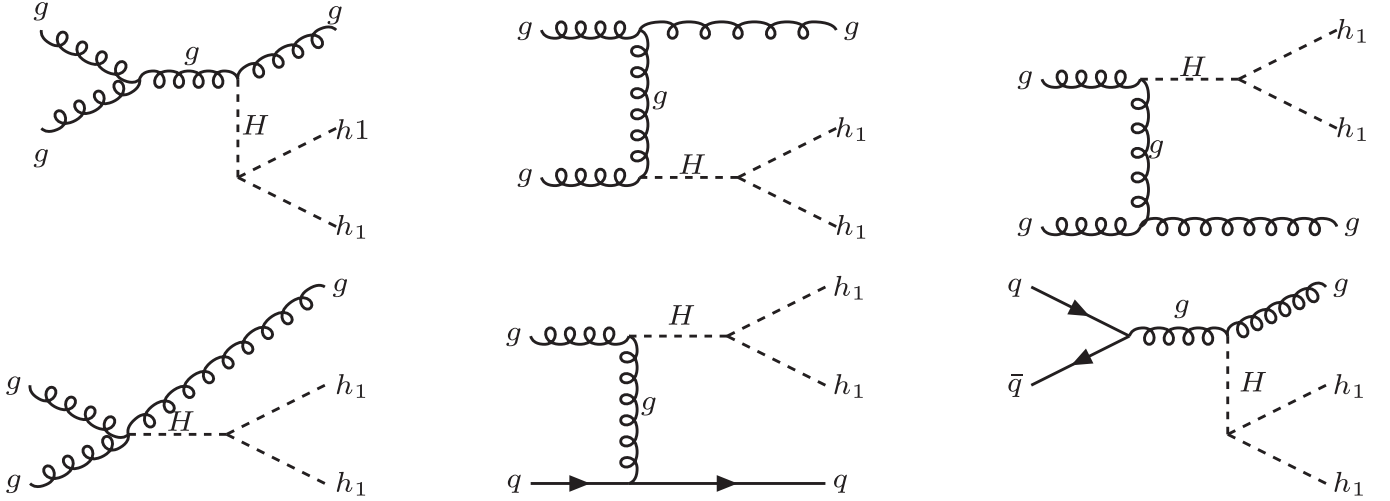
FIG. 4.   Feynman diagrams for the $gg \to h_1 h_1 + g$ process contributing to the monojet signature.

below about 0.05, which is crucial for one of the main signatures of DM searches at the LHC which we discuss below.[2]

The asymmetric picture with respect to negative and positive values of λ_{345} is even more pronounced in the case of these latest results as one can clearly see the white funnel region excluded for $\lambda_{345} < 0$. The reason for this is again the negative interference between DM annihilation into EW gauge bosons via Higgs boson exchange and $h_1 h_1 VV$ quartic couplings described above; in this funnel region, this negative interference brings the DM relic density up, which in turn increases the DM DD rates.

One should note that, though constraints from DM DD and invisible Higgs decay on $|\lambda_{345}|$ dominate the one from vacuum stability, the latter sets the most strict upper bound on λ_{345} for $M_{h_1} \simeq M_H/2$. In this region, the invisible Higgs decay is suppressed by the phase space, while DM DD rates rescaled by relic density are suppressed because Ωh^2 is driven to low values in this parameter space, which is dominated by $h_1 h_1 \to H$ resonant annihilation. Therefore, the constraint from vacuum stability which becomes important in this region limits $\lambda_{345} \lesssim 1.6$ as follows from Eq. (7).

III. MONOJET SIGNATURES AT THE LHC

The i2HDM exhibits different collider signatures, which can potentially be accessible at the LHC. In this analysis,

we will focus on monojet final states, which arise from $gg \to h_1 h_1 + g$, $qg \to h_1 h_1 + q$, and $q\bar{q} \to h_1 h_1 + g$ processes, to which we will refer cumulatively as the $h_1 h_1 j$ process. The corresponding Feynman diagrams are presented in Fig. 4.

For this signature, and for $M_{h_1} > M_H/2$, the relevant nontrivial parameter space is one dimensional and corresponds to the DM mass, M_{h_1}, since the production cross section is proportional to $(\lambda_{345})^2$. For $M_{h_1} < M_H/2$, however, the situation can be different, for two reasons: a) only $H \to h_1 h_1$ takes place, so that the cross section is defined by the production of the SM-like Higgs times $\text{Br}(H \to h_1 h_1)$, which is a function of λ_{345} and M_{h_1}, and b)
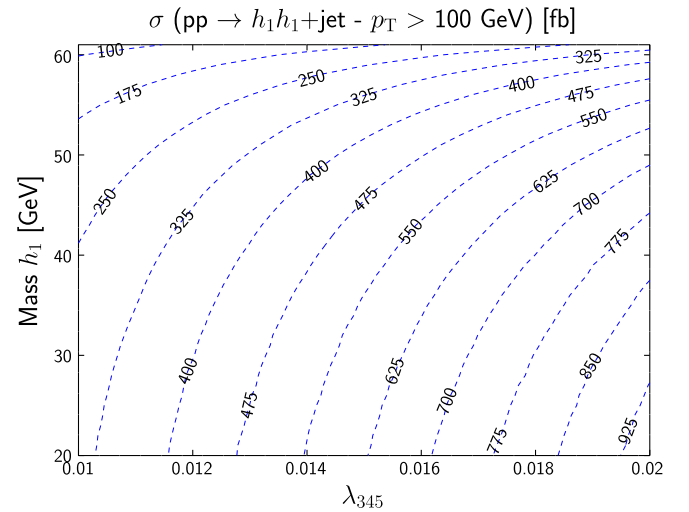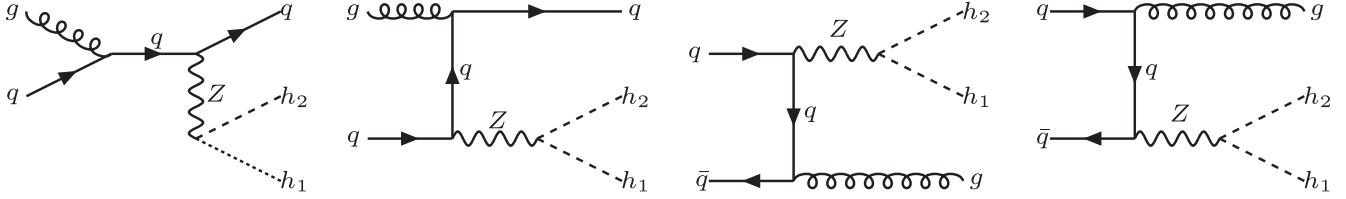

FIG. 5.   Cross sections vs DM mass M_{h_1} and coupling constant λ_{345} for the monojet process $h_1 h_1 j$ at the LHC@13 TeV. The mass of the h_2 particle is set to $M_{h_2} = 200$ GeV. Here, the cross section was evaluated for the initial cut on $p_T^{\text{jet}} > 100$ GeV.

---

[2]One should note that in Ref. [56] the authors have also analysed i2HDM parameter space using XENON1T (2017) constraints. However, the pattern of their surviving parameter space is quite different in some specific regions. For example, for M_{h1} just above $M_H/2$, we have found parameter space with $\lambda_{345} \simeq 1$, $M_{h1} \simeq M_{h2}$, which satisfy experimental limits and which have DM relic density below the Planck upper limit primarily because of the strong $h_1 - h_2$ coannihilation channel. We believe that this region was missed in Ref. [56].

FIG. 6.   Feynman diagrams for the $q\bar{q} \to h_1 h_2 + g$ ($gq \to h_1 h_2 + q$) process.

both $H \to h_1 h_1$ and $H \to h_2 h_2$ contribute to the invisible Higgs decay, which then implies that both $h_1 h_1 j$ and $h_2 h_2 j$ will contribute to the same signature (for a few giga-electron-volts mass difference between h_2 and h_1, $h_2 \to h_1 f \bar{f}$ is invisible because of the soft fermions f in the final state), the cross section of which is defined by the production of the SM-like Higgs state times $(\text{Br}(H \to h_1 h_1) + \text{Br}(H \to h_2 h_2))$, which is a function of λ_{345}, M_{h_1} as well as M_{h_2}.

In Fig. 5, we present the cross sections for the monojet process $h_1 h_1 j$ at the LHC@13 TeV in the (M_{h_1}, λ_{345}) plane. The monojet cross section was evaluated with the initial cut on $p_{\mathrm{T}}^{\mathrm{jet}} > 100$ GeV, λ_{345} has been chosen to be in the range [0.01, 0.02], M_{h_1} has been chosen in the range [20, 60] GeV, and M_{h_2} has been fixed to 200 GeV. We can see that, for this range of parameters, the cross section rate is between 100 and 1000 fb, which gives us a strong motivation to probe this signal at the LHC. For this and the following parton level calculations and simulations, we have used the HEPMDB site [57], the CALCHEP package [48], and the NNPDF23LO (AS_0130_QED) parton distribution function (PDF) set [58] with both the factorization and renormalization scales set to the transverse mass of the final state particles.

An important remark is that the mass of the top quark in the loop which defines the ggH coupling can be less than the energy scale of the $h_1 h_1 j$ process which is related to the jet transverse momentum, p_T^{jet}. Hence, in the region of high p_T^{jet}, one should check the validity of the EFT approach based on the heavy top-quark approximation, which is often used for simplification. This is the subject of the next section.

There is one more process that potentially contributes to the monojet signature in the i2HDM, namely, $q\bar{q} \to h_1 h_2 + g$ ($gq \to h_1 h_2 + q$), which we will refer to as the $h_1 h_2 j$ process. Feynman diagrams for this process are presented in Fig. 6. This process contributes to the monojet signature when the mass splitting between h_1 and h_2 is small, of the order of few giga-electron-volts. In this case, h_2 will decay to h_1 and soft jets or leptons from a virtual Z which escapes detection. In spite of the fact that there is one mediator for this process, i.e., the Z boson, one can see that t- and s-channel topologies with a light quark in the propagator make this process different from simplified models with

fermionic DM and a vector mediator, which have been studied so far in the literature, so it is worth exploring it in detail.

The parameter space for this process is characterized by two variables, M_{h_1} and M_{h_2}, which fix its cross section for a given collider energy. It is also convenient to use $\Delta M = M_{h_2} - M_{h_1}$, the mass difference between the two particles, instead of M_{h_2}. In Fig. 7, we present the cross section for the $h_1 h_2 j$ process in the $(M_{h_1}, \Delta M)$ plane. The cross section has been evaluated with an initial cut, $p_{\mathrm{T}}^{\mathrm{jet}} > 100$ GeV. One can see that, in this plane, the pattern of the cross section isolevels takes a simple form. One can also note that in case of $M_{h_1} \simeq 50$–60 GeV and small ΔM the cross section is of the order of 100 fb, which could be in the region of the LHC sensitivity. This cross section is comparable to that of the $h_1 h_1 j$ process for $\lambda_{345} = 0.01$ and the same mass, which makes this kind of process important for the parameter space region where λ_{345} is small. It is important to stress that the cross section for the $h_1 h_2 j$ process is independent of λ_{345}; therefore, this process
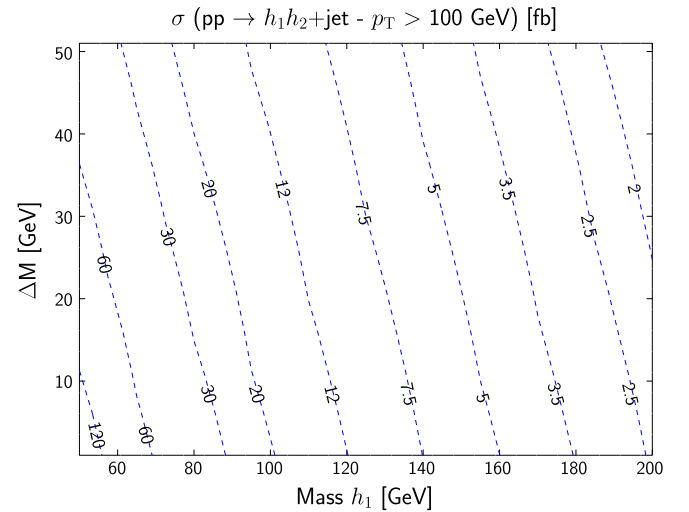

FIG. 7.   Cross section vs DM mass M_{h_1} and $\Delta M = M_{h_2} - M_{h_1}$ for the monojet process $h_1 h_2 j$ at the LHC@13 TeV. This process gives rise to a monojet signal if the mass difference ΔM is small enough, such that the decay $h_2 \to h_1 + X$ gives rise only to $E_{\mathrm{T}}^{\mathrm{miss}}$ + soft undetected leptons or jets. Here, the cross section was evaluated for the initial cut $p_{\mathrm{T}}^{\mathrm{jet}} > 100$ GeV.
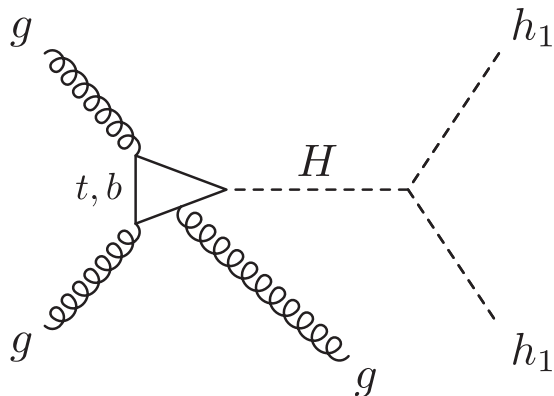
FIG. 8. Representative Feynman diagram for the one-loop (top- and bottom-quark) induced $gg \rightarrow h_1 h_1 g$ process under study.

would provide a probe of the i2HDM parameter space, which is complementary to the $h_1 h_1 j$ process.[3]

A. Validity of the effective *ggH* vertex approach

The SM ggH vertex is dominantly generated by the top-quark loop (with a small bottom-quark contribution). It is known that integrating out the top quark is a good approximation for Higgs production processes when considering inclusive rates, as long as the Higgs boson is not far off shell or with high transverse momentum. The literature on this subject is vast, and we refer the reader to the corresponding sections in Ref. [59] and references therein. In case of our study, however, the selection of large transverse momentum of the jet (done to increase the signal-to-background ratio), which is typically bigger then the top-quark mass, is likely to lead to the breakdown of the heavy top-quark approximation.

From one of the representative one-loop diagrams presented in Fig. 8 for the $gg \rightarrow h_1 h_1 g$ process, one can see that a high p_T jet emitted from the top-quark loop can "resolve" the top quark in the loop if the transverse momentum of the jet is large enough. This effect is crucial since the monojet p_T and E_T^{miss} distributions from the EFT approximation (which one could be tempted to use for the sake of simplicity) could be different from those described by the exact loop calculation. This is even more crucial for us, due to the E_T^{miss} shape-analysis techniques which we use in our study. Therefore, we have compared the E_T^{miss} shapes for the events simulated using the EFT heavy top-quark

approximation to those from the exact one-loop calculation. For this purpose, we have simulated the process of Higgs boson production in association with a jet and scanned over the mass of the Higgs boson, corresponding to the different invariant masses of the DM pair.

For this specific study, our simulations have been performed with MADGRAPH5 [60,61] using the NNPDF2.3 PDF set [58]. We have compared results for two models: MADGRAPH5 native SM implementation with the effective ggH vertex and the SM at one-loop implementation. Using this setup, we have scanned over a range of Higgs boson masses and compared the Higgs boson p_T and η distributions for the effective ggH vertex and one-loop level implementations. The results presented in Fig. 9 are evaluated for different benchmarks, corresponding to different Higgs masses (for both effective vertex and one-loop simulations) and with contributions of either top or bottom quarks, or both. We have applied an initial cut $p_T^{\mathrm{jet}} > 200$ GeV for this study. The differences between effective vertex and one-loop distributions are quite large for large transverse momenta, and the role of the bottom quark in the loop is—as one may expect—rather marginal. The pseudorapidity distribution is not affected as much. It is, however, interesting to notice that larger invariant masses shift the distribution from a central-peaked shape to a more forward-backward behavior. For a sanity check, we have also evaluated the effect of setting the top-quark mass to 10 TeV in the one-loop calculation, so that it can be effectively cross-checked with the effective vertex results, and as one can see, indeed it agrees with those.

As a result of this comparison, we have defined a k-factor,

$$k_f = \frac{\sigma(pp \rightarrow h_1 h_1 j)_{\mathrm{one-loop}}}{\sigma(pp \rightarrow h_1 h_1 j)_{\mathrm{EFT}}}, \qquad (9)$$

which provides correspondence between the effective vertex and one-loop results in the p_T distribution of the Higgs boson as a function of two variables: E_T^{miss} and $M_{(\mathrm{DM,DM})}$ (the invariant mass of the DM pair). This k-factor is pictorially presented in Fig. 10. One can see that, for large E_T^{miss} values, the effect of the breakdown of the effective vertex approximation is dramatic. For example, for $E_T^{\mathrm{miss}} = 1$ TeV, the effective vertex approximation overestimates the one-loop result by 1 order of magnitude, i.e., $k_f \simeq 0.1$. At the same time, for smaller values of E_T^{miss}, the effective vertex approximation can even underestimate the one-loop result, which happens for large values of the $M_{(\mathrm{DM,DM})}$ invariant mass of the DM pair; for example, for $E_T^{\mathrm{miss}} = 300$ GeV and $M_{(\mathrm{DM,DM})} = 500$ GeV, one finds $k_f \simeq 1.5$.

It is finally very important to stress that the k-factor which was found in two recent studies at next-to-leading order in QCD [62,63] is very close (within few percent) to

---

[3] On similar footing, we should finally mention that the monojet signature emerging from the i2HDM also sees a component in which an h_2 pair is produced, when ΔM is very small. The production topologies of this process, henceforth $h_2 h_2 j$, are the same as those for the $h_1 h_1 j$ case, though the yield is generally smaller. We nonetheless include this channel in our simulations, yet we will not dwell on it separately.
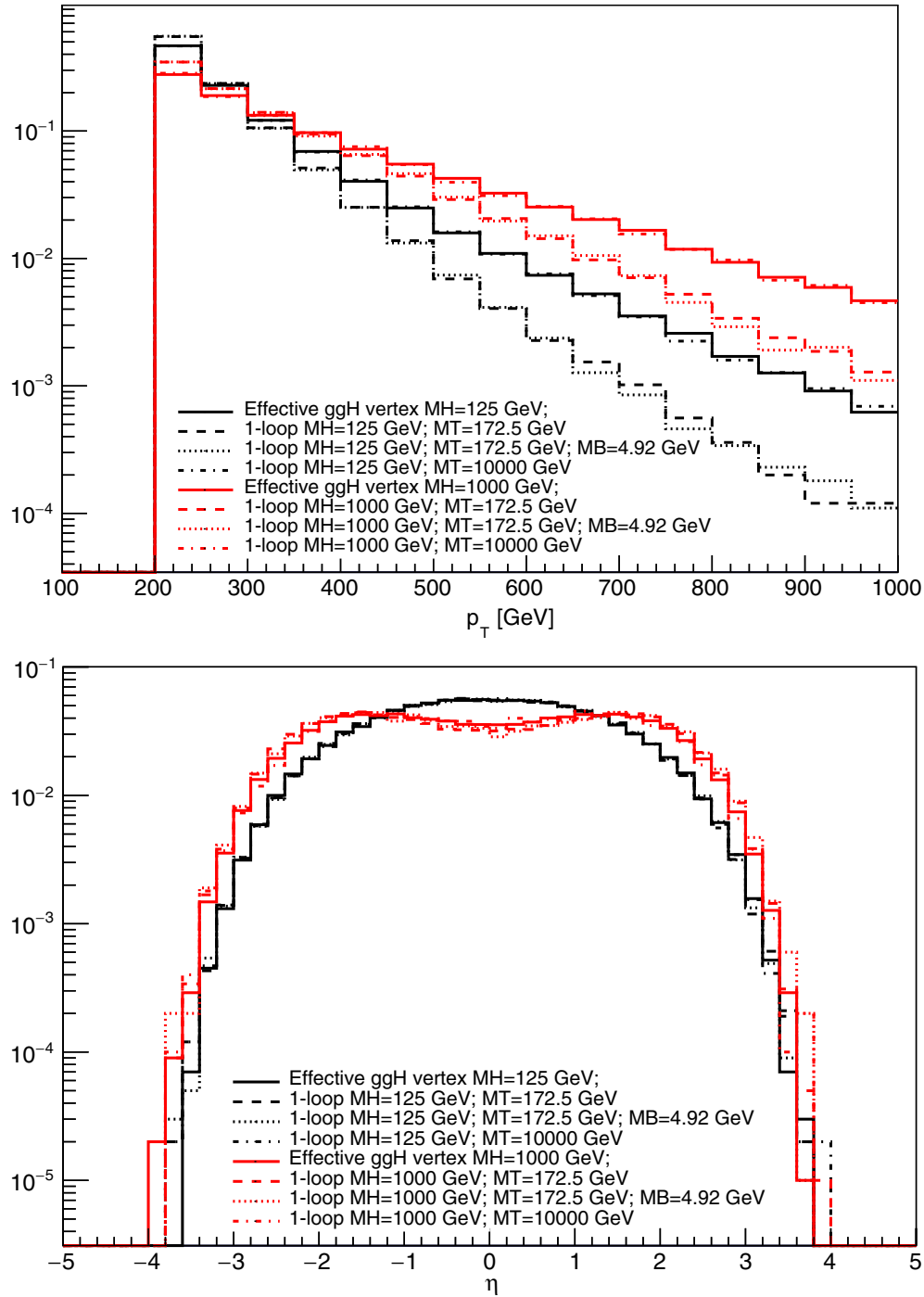
FIG. 9.   Shape of transverse momentum (top panel) and pseudorapidity (bottom panel) distributions for a Higgs boson produced in association with one jet. Solid curves correspond to the distributions for the effective ggH vertex approximation, dashed ones are for the one-loop result with only the top quark in the loop, dotted ones are for the one-loop result with both top and bottom quarks in the loop, and dot-dashed ones are for a very heavy quark in the loop ($m_t = 10$ TeV) for the purpose of cross-checking the effective ggH vertex approximation. Black and red colors correspond to $M_{(DM,DM)} = 125$ and 1000 GeV, respectively.

the one we have found here at the leading order (LO) only (see also Ref. [64] where similar work is presented). Hence, based on our findings in this section, for our analysis below, we use one-loop results (i.e., at LO in QCD) and take into account the contributions from both top and bottom quarks.

B. LHC potential to probe the i2HDM parameter space

1. Benchmarks

Taking into account all the constraints, and especially the recent XENON1T ones, we suggest a set of six benchmark
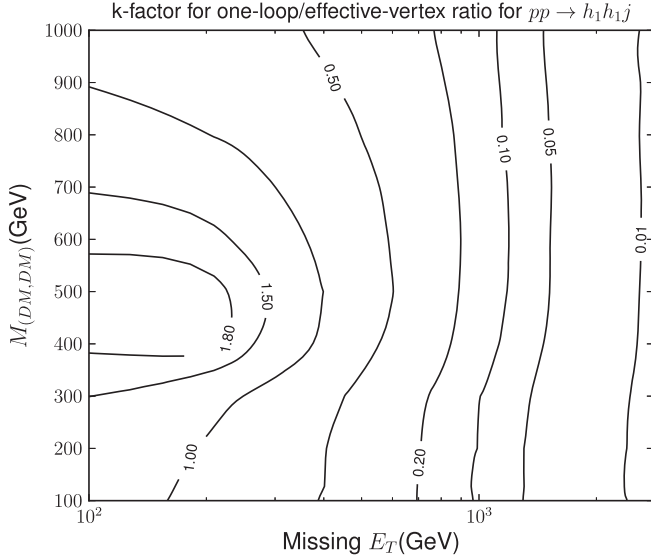
FIG. 10.   The k-factor k_f defined in the text as a function of the E_T^{miss} and invariant mass of the DM pair. The k-factor values are indicated in the contour lines.

(BM) points, BM1 to BM6, summarized in Table I and described below:

(i) *BM1*: Both M_{h_1} and M_{h_2} are below $M_H/2$ contributing to about 20% of the invisible Higgs boson decay and yielding about 800 fb of cross section for

the monojet signature (which is high enough to be tested at the HL-LHC as we will discuss below) coming from the cumulative sum of the $h_1 h_1 j$, $h_1 h_2 j$, and $h_2 h_2 j$ processes. To measure the XENON1T sensitivity, we use the SI DM scattering rate on the proton (σ_{SI}^p) accompanied by its ratio to the experimental limit from XENON1T, following rescaling with the relic density, $R_{SI}^{XENON1T} = (\sigma_{SI}^p/\sigma_{SI}^{XENON1T}) \cdot (\Omega_{DM}/\Omega_{DM}^{Planck})$, which is equal to 0.29 for this benchmark, i.e., about a factor of 3 below the current XENON1T sensitivity. The DM relic density for this point is below the Planck constraints because of the $h_1 h_2$ coannihilation.

(ii) *BM2*: Only M_{h_1} is below $M_H/2$, and the value of λ_{345} is chosen to be small enough for the DM relic density to match both the upper and lower Planck constraints. In this case, the invisible Higgs boson decay to DM is only 2%, and the respective rate of the $h_1 h_1 j$ monojet signal is only 74.6 fb. This point, with $R_{SI}^{XENON1T} = 0.75$, is likely to be tested with future DM DD experiments since its value is not far from the present XENON1T limit.

(iii) *BM3*: Only $M_{h_1} = 60$ GeV is below $M_H/2$, but $M_{h_2} = 68$ GeV is quite close to it. Because of the large invisible Higgs boson decay to DM with $Br(H \to h_1 h_2) = 0.25\%$, the leading signal at the LHC will be a monojet from $h_1 h_1 j$, with a rate above

TABLE I.   BM points from the i2HDM parameter space together with corresponding observables: DM relic density ($\Omega_{DM} h^2$), SI DM scattering rate on the proton (σ_{SI}^p) accompanied by its ratio to the experimental limit from XENON1T following rescaling with the relic density, $R_{SI}^{XENON1T} = (\sigma_{SI}^p/\sigma_{SI}^{XENON1T}) \cdot (\Omega_{DM}/\Omega_{DM}^{Planck})$ plus the LHC cross sections at the LHC@13 TeV with a $p_T^{jet} > 100$ GeV cut applied.

BM	1	2	3	4	5	6
M_{h_1} (GeV)	55	55	60	60	70	80
M_{h_2} (GeV)	62	110	68	68	78	81
M_{h_+} (GeV)	120	120	100	100	78	81
λ_{345}	0.01	0.0065	0.033	0.0001	0.01	0.0
λ_2	1.0	1.0	1.0	1.0	1.0	1.0
Γ_{h_2} (GeV)	1.307×10^{-8}	2.926×10^{-4}	2.564×10^{-8}	2.564×10^{-8}	2.627×10^{-8}	7.314×10^{-13}
Γ_{h_+} (GeV)	1.549×10^{-3}	9.905×10^{-4}	1.137×10^{-4}	1.137×10^{-4}	3.666×10^{-8}	7.587×10^{-13}
$\Omega_{DM} h^2$	1.78×10^{-2}	1.10×10^{-1}	1.37×10^{-4}	1.04×10^{-1}	4.56×10^{-2}	7.52×10^{-3}
σ_{SI}^p (pb)	1.75×10^{-10}	7.37×10^{-11}	1.59×10^{-9}	1.46×10^{-14}	1.07×10^{-10}	0.0
$R_{SI}^{XENON1T}$	0.29	0.75	0.020	1.4×10^{-4}	0.45	0.0
$Br(H \to h_1 h_1)$	4.15×10^{-2}	0.022	0.25	3.1×10^{-6}	0.0	0.0
$Br(H \to h_2 h_2)$	1.59×10^{-1}	0.0	0.0	0.0	0.0	0.0
$\sigma_{LHC@13\,TeV}$ (fb)						
$h_1 h_1 j$	1.46×10^2	74.6	857	1.08×10^{-2}	4.96×10^{-3}	0.0
$h_2 h_2 j$	5.47×10^2	3.88×10^{-1}	3.06×10^{-1}	8.00×10^{-2}	5.50×10^{-2}	5.34×10^{-4}
$h_1 h_2 j$	1.04×10^2	34.1	77.4	77.0	49.6	39.0
$h_1 h^\pm j$	49.2	49.0	65.0	65.5	83.9	66.5
$h_2 h^\pm j$	44.9	24.7	58.0	57.9	72.1	65.4
$h^\pm h^\pm j$	13.0	13.0	20.9	16.2	39.2	35.3

800 fb, complemented by the h_1h_2j process with rate 77.4 fb, which are high enough to be tested at the HL-LHC.

(iv) *BM4*: $M_{h_1} = 60$ GeV and $M_{h_2} = 68$ GeV as in BM3, but λ_{345} is chosen to be low enough such that the DM relic density, governed by h_1h_2 coannihilation, is within the upper and lower Planck constraints. This point is unlikely to be tested by DD DM experiments in the near future, while the LHC could potentially test it shortly via a combination of h_1h_2j, $h_1h^{\pm}j$, $h_2h^{\pm}j$, and $h^{\pm}h^{\pm}j$ signatures, which are outside the scope of this paper.

(v) *BM5*: With all inert scalars close in mass, $M_{h_1} = 70$ GeV, $M_{h_2} = 78$ GeV, $M_{h^{\pm}} = 78$ GeV, so all h_1h_2j, $h_1h^{\pm}j$, $h_2h^{\pm}j$, and $h^{\pm}h^{\pm}j$ channels contribute to the monojet signature (since both h_2 and $h^{\pm}$ promptly decay to h_1 and soft leptons escaping detection) with a total rate of about 250 fb, which is close to the exclusion limit at the HL-LHC as we will see below.

(vi) *BM6*: Masses for all inert scalars are even closer to each other in comparison to BM5, as $M_{h_1} = 80$ GeV, $M_{h_2} = 81$ GeV and $M_{h^{\pm}} = 81$ GeV. Since $\lambda_{345} = 0$ the rates of h_1h_1j and h_2h_2j processes are vanishing. With this configuration all h_1h_2j, $h_1h^{\pm}j$, $h_2h^{\pm}j$, and $h^{\pm}h^{\pm}j$ channels contribute to the monojet signature with a total rate of about 210 fb, again close to the exclusion limit at the HL-LHC.

The masses of DM for BM1–BM6 were chosen below 100 GeV in anticipation of the LHC sensitivity to the parameter space, which we present below. At present, the LHC experimental collaborations ATLAS and CMS do not have specific searches for the i2HDM; however, the results for generic DM searches in the jet $+ E_T^{\text{miss}}$ channel can be reinterpreted in the context of such a model. In order to compare the i2HDM to those limits, the following procedure is followed:

(i) The matrix elements that describe the hard interaction are simulated with CALCHEP, and event samples for different values of M_{h_1} are produced. In order to concentrate on a region of phenomenological interest and simulate events with enhanced statistics, a lower threshold on the final state parton (either q or g) is set at $p_T > 100$ GeV. The event samples are produced in the Les Houches Event format for further processing.

(ii) In order to accurately describe the p_T distribution, each event is weighted with the k-factor estimated in the previous section, according to its parton p_T and the invariant mass of the DM-DM system.

(iii) Each event sample is then passed to PYTHIA8.2 [65,66] for the proper treatment of parton showering, hadronization, and underlying event effects. The aforementioned NNPDF set is again deployed through the LHAPDF6 tool [67].

(iv) The DELPHES3 framework for fast simulation of generic collider experiments [68] is used to simulate the event reconstruction by the CMS experiment. Specifically, the detector parametrization for CMS described as standard in the card DELPHES_CARD_CMS.TCL from the DELPHES distribution is used.

(v) A set of selection criteria is applied to the simulated reconstructed events. In the experimental collaborations, these criteria aim to reduce both the SM backgrounds (mainly composed of inclusive W/Z-boson production) and instrumental noise that mimics the appearance of a single, highly energetic jet in the event. We disregard the effect of the latter phenomenon in our analysis, though.

After the fast detector level simulation described above, we performed an analysis of the missing transverse momentum distribution E_T^{miss} of the signal events. We compare the E_T^{miss} distribution predicted by a given signal sample to the standard model background prediction. That background prediction is a fundamental ingredient for our analysis; it can either be explicitly given by the experimental collaborations or estimated by an explicit calculation of the inclusive W/Z-boson production cross section shape. For each signal sample, we set upper limits on the production cross section of the monojet process. We compute the limits following an asymptotic approximation to the modified frequentist prescription known as the CL_S technique [69,70], in which systematic uncertainties are treated as nuisance parameters through use of the profile likelihood ratio. The only systematic uncertainty we consider in our analysis is the uncertainty in the background prediction. Throughout our study, the THETA framework [71] for modeling, and inference is used for all statistical analyses and limit-setting procedures.

We study the jet $+ E_T^{\text{miss}}$ signature from two signal processes, h_1h_1j and h_1h_2j, in the presence of a small (a few GeV) $M_{h_2} - M_{h_1}$ mass gap making h_1h_2j to contribute to the monojet signature. In our study, we analyze h_1h_1j and h_1h_2j separately for two reasons: a) the rate of these processes depends upon different parameters, so they complement each other as i2HDM parameter space probes, and b) these processes have different shapes in the E_T^{miss} distribution because of the different nature and mass of the mediators.

2. Results from Run 2 data

At the beginning of Run 2, the LHC@13 TeV delivered a total integrated luminosity of 4.2 fb^{-1}. The CMS Collaboration released a public result where 2.3 fb^{-1} of data were used to search for DM production in association with jets or hadronically decaying vector bosons [72]. Henceforth, we will refer to this result as the "CMS Run 2 analysis." Supplementary material—data and Monte Carlo

TABLE II.   Initial selection cuts for the CMS Run 2 monojet analysis at $\sqrt{s} = 13$ TeV [72]. Jets considered for the jet multiplicity and angular configuration selections are required to have $p_T^{jet} > 30$ GeV and $|\eta^{jet}| < 2.5$.

Quantity	Selection
Leading jet p_T	> 100 GeV
Leading jet $|\eta|$	< 2.5
E_T^{miss}	> 200 GeV
$\Delta\phi(E_T^{miss}, jet_{1...4})$	> 0.5

background distributions as well as their uncertainties— were made available by the collaboration and used to set limits on the i2HDM. Table II summarizes the experimental selection used for the CMS result, while Table III presents the data used for our study at 13 TeV.

The main change for the Run 2 selection was the update of the angular discriminant to suppress QCD multijet contributions, whereas in Run 1, a strict requirement was imposed on the jet multiplicity and leading jets azimuthal distance in Run 2 CMS opted instead for an overall requirement of azimuthal separation between the measured E_T^{miss} and the four leading hadronic jets. The selection efficiency for both the h_1h_1j and h_1h_2j processes can be seen in Fig. 11 and is around 10%–25% for the former and 18%–40% for the latter. We can understand this difference by noticing that h_1h_2j production is mediated by a Z boson while h_1h_1j production is mediated by the

TABLE III.   SM background prediction and observed data for the CMS Run 2 monojet analysis at $\sqrt{s} = 13$ TeV [72] as a function of the E_T^{miss} variable.

| Bin range (GeV)	SM background	Observed data
200–230	28654 ± 171	28601
230–260	14675 ± 97	14756
260–290	7666 ± 68	7770
290–320	4215 ± 48	4195
320–350	2407 ± 37	2364
350–390	1826 ± 32	1875
390–430	998 ± 23	1006
430–470	574 ± 17	543
470–510	344 ± 12	349
510–550	219 ± 9	216
550–590	134 ± 7	142
590–640	98.5 ± 5.8	111
640–690	58.0 ± 4.1	61
690–740	35.2 ± 2.9	32
740–790	27.7 ± 2.7	28
790–840	16.8 ± 2.2	14
840–900	12.0 ± 1.6	13
900–960	6.9 ± 1.2	7
960–1020	4.5 ± 1.0	3
1020–1160	3.2 ± 0.9	1
1160–1250	2.2 ± 0.7	2
1250—inf	1.6 ± 0.6	3
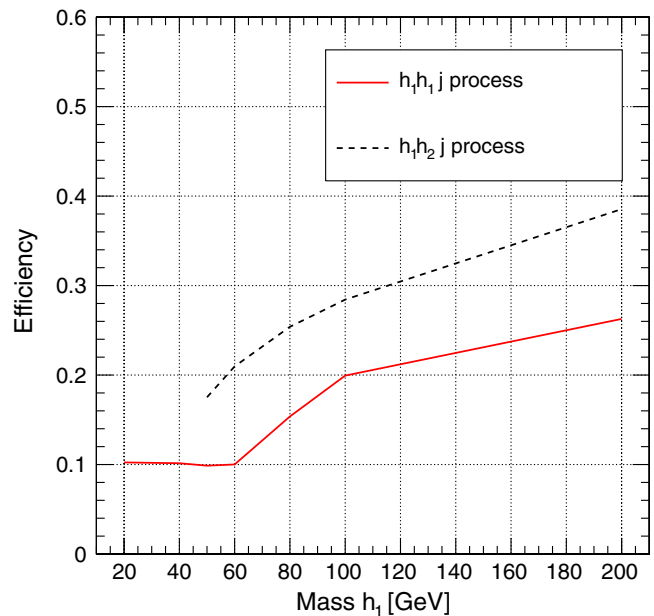
FIG. 11.   Efficiency of the selection criteria described in Table II, on the simulated reconstructed events, for h_1h_1j (solid red line) and h_1h_2j (dashed black line). Here, $\sqrt{s} = 13$ TeV.

SM-like Higgs boson, which leads to a different E_T^{miss} spectrum. Figure 12 presents the comparison of the E_T^{miss} distributions for different DM masses for the signal from the h_1h_1j (left panel) and h_1h_2j (right panel) processes as well as for the background. One can notice that the E_T^{miss} distribution for the h_1h_2j signal is indeed harder than the one for the h_1h_1j case. This difference in E_T^{miss} shapes is related to the difference in the invariant mass of DM pair distributions, for h_1h_2j and h_1h_1j signals; as discussed in Ref. [13], a scalar mediator defines a softer invariant mass of the DM pair than a vector mediator (for similar masses), while the invariant mass of the DM pair in its turn is correlated with the shape of the E_T^{miss} distribution.

It can be observed from Fig. 12 that the E_T^{miss} spectrum of the signal is harder than that of the background for the whole range of DM masses sampled, especially for the large values, which agrees with the findings of Ref. [13], where it was shown that distributions at larger values of $M_{(DM,DM)}$ have a flatter E_T^{miss} shape. Eventually, for higher values of M_{h_1}, $M_{(DM,DM)}$ will also be higher. This suggests two strategies for the signal and background comparison. A simpler analysis would be a so-called *counting experiment*, where a lower E_T^{miss} threshold ("cut") is defined and the spectrum is integrated above that value. This procedure produces a single event yield (with uncertainty) for both signal (N_{sig}) and background (N_{bkg}), and in the case of an observed limit, the total number of observed events (N_{obs}) would also be available. Those are input to the limit-setting technique described in the previous section, through a single likelihood $\mathcal{L}(N_{sig}, N_{bkg}, N_{obs})$. A more sophisticated
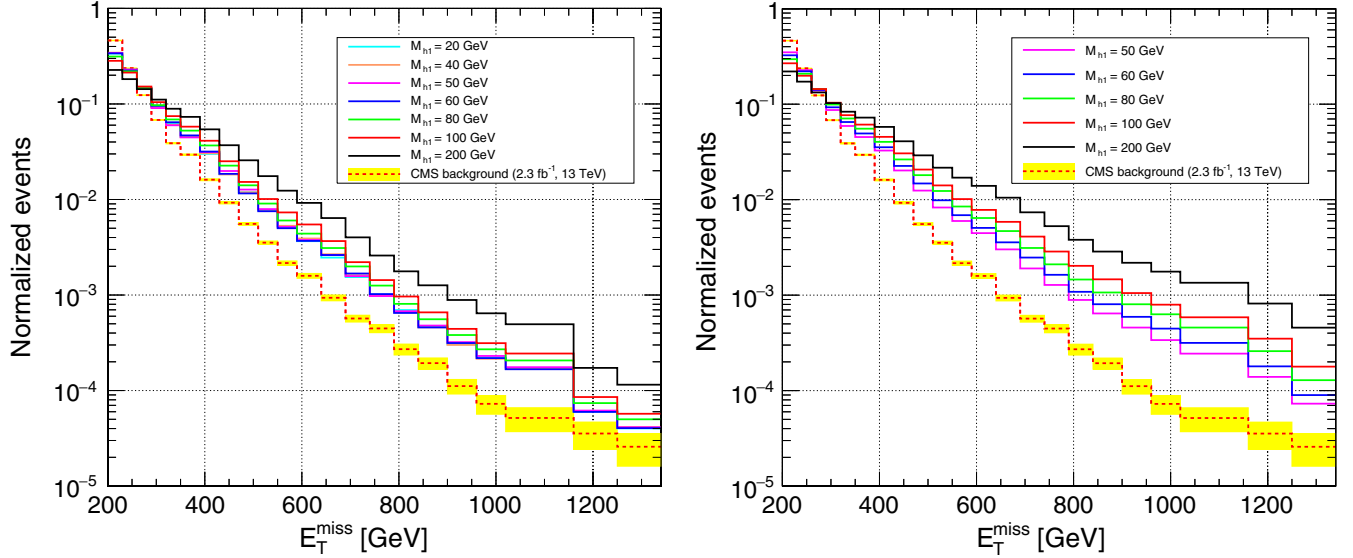
FIG. 12.   Comparison of E_T^{miss} distributions between signals, for $h_1 h_1 j$ (left) and $h_1 h_2 j$ (right), for various DM masses, alongside the estimated (by CMS) experimental background for $\sqrt{s} = 13$ TeV.

analysis, in contrast, could take into account the coherent enhancement over all the E_T^{miss} spectrum that the presence of a signal would entail. In this strategy, the binned likelihood is written as the product of the single likelihoods of each bin over the relevant E_T^{miss} range. This will be called the *shape analysis* strategy. The CMS Run 1 analysis [73] used a series of counting experiments with different E_T^{miss} ranges, while the CMS Run 2 analysis employs a shape analysis. Figure 13 shows, for our signal samples and the background estimates from the CMS Run 2 analysis, the difference among four different analysis strategies: three counting experiments, with respective E_T^{miss} cuts of 200, 470, and 690 GeV, and a shape analysis with a lower threshold of 200 GeV. One can see that higher E_T^{miss} thresholds in the counting experiment make the expected limit become worse, while the shape analysis is able to leverage the coherent enhancements in all bins of E_T^{miss} that arises from the signal presence to set a better limit, an order of 30% improvement. We will therefore adopt the shape analysis strategy for the rest of this study.

Figure 14 shows the 95% confidence level (CL) expected and observed exclusion limits as a function of M_{h_1} derived using the CMS 13 TeV background prediction and observed data with the Run 2 selection as described in Table II. In the left panel, we show the limit for the $h_1 h_1 j$ process. In order to compare with the actual signal rate, we show two signal lines for different values of λ_{345}. A red solid line presents the i2HDM cross section for $\lambda_{345} = 0.019$ that is near the maximum allowed by the Higgs invisible decay search, when $M_{h_1} < M_H/2$. In this region, the SM-like Higgs boson is produced on shell, which enhances substantially the production cross section, and we can further notice a steep drop of the latter for $M_{h_1} > 60$ GeV. In contrast, for

$M_{h_1} > M_H/2$, there is no bound on λ_{345} from the Higgs invisible decay width, and the cross section scales with λ_{345} squared. We show with a blue dashed line the expected i2HDM cross section for maximally allowed λ_{345} by the present data; it reaches 1.6 times the value that is around the
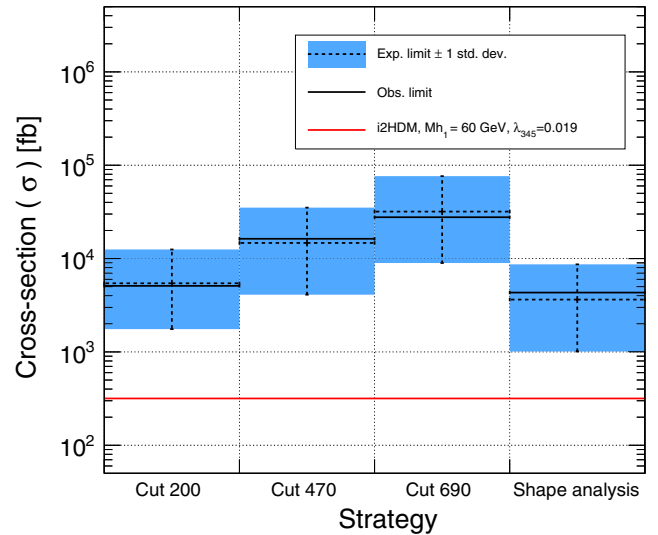

FIG. 13.   Expected and observed limits for four different analysis strategies: three counting experiments, with lower thresholds of 200, 470 and 690 GeV, and a shape analysis with a lower threshold of 200 GeV. The counting experiments are able to set expected limits of 5.44 pb, 14.7 pb, and 31.9 pb, respectively, while the shape analysis is able to set an expected limit of 3.64 pb, a 30% improvement over the counting experiment with lowest threshold. The red line is for the $h_1 h_1 j$ process with $M_{h_1} = 60$ GeV, $M_{h_2} = 200$ GeV, $\lambda_{345} = 0.019$, giving a cross section of 0.317 pb.
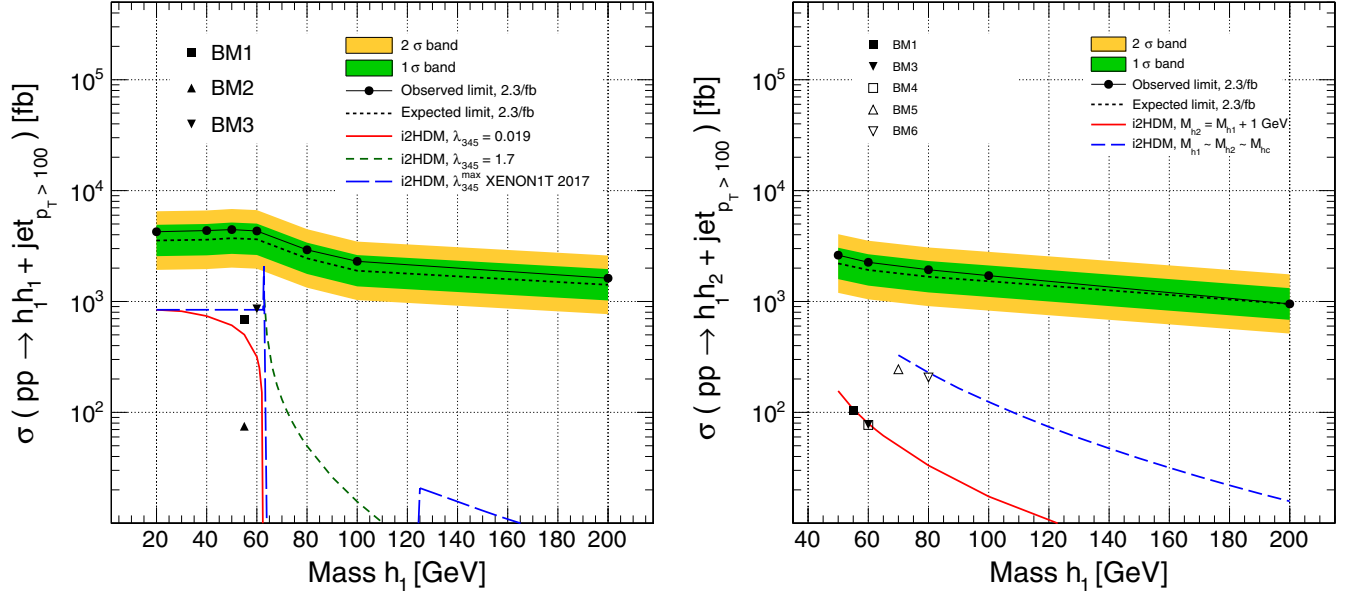
FIG. 14.   Left: Expected and observed limits on the $h_1 h_1 j$ process for 2.3 fb^{-1} of 13 TeV pp collision data. The red solid line is the cross section for the parameter set $\lambda_{345} = 0.019$, $M_{h_2} = 200$ GeV while the green short dashed line is the cross section for the parameter set $\lambda_{345} = 1.7$, $M_{h_2} = 200$ GeV. The blue dashed line is the combined contribution $h_1 h_1 j + h_1 h_2 j$ that is still allowed by XENON1T data (see text). Right: Expected and observed limits on the $h_1 h_2 j$ process for 2.3 fb^{-1} of 13 TeV pp collision data. The red solid line is the cross section for $M_{h_2} = M_{h_1} + 1$ GeV. The blue short dashed line is the cross section for a full degeneracy between h_1, h_2 and h_c, where additional processes involving the charged scalar could mimic the $h_1 h_2 j$ process. The cross section is plotted for values of M_{h_1} larger than ∼70 GeV to comply with the LEP bound on the charged Higgs mass [45]. In all cases the isolated symbols represent the benchmark points discussed in Table I. All cross sections are given for a $p_T^{\rm jet} > 100$ GeV requirement.

maximum for $M_{h_1} \simeq M_H/2$ allowed by vacuum stability. Outside of the $M_{h_1} \simeq M_H/2$ region, λ_{345} is strongly excluded by XENON1T data; e.g., in the interval 65 GeV $< M_{h_1} <$ 70 GeV, the only values of $\lambda_{345} \lesssim$ 0.025 are allowed. We can see that, for the 2.3 fb^{-1} data set, we exclude the $h_1 h_1 j$ process cross sections in the range of 4.3–1.6 pb for M_{h_1} in the range 20–200 GeV, which does not exclude the i2HDM even for the highest allowed value of λ_{345}. For the $h_1 h_2 j$ process, we exclude cross sections in the range of 2.6–0.95 pb for M_{h_1} in the range 50–200 GeV, also not enough to set relevant limits on the i2HDM.

When $M_{h_1} \simeq M_{h_2}$, h_2 will decay to h_1 plus very soft products; thus, $h_1 h_1 j$, $h_2 h_2 j$, and $h_1 h_2 j$ production will contribute to the jet + $E_T^{\rm miss}$ signature. The $h_2 h_2 j$ and $h_1 h_1 j$ channels proceed via the same mediator and can be combined since they have the same $E_T^{\rm miss}$ shape (for small values of $\Delta M = M_{h_2} - M_{h_1}$). We indicate the predicted combined $h_1 h_1 j$ and $h_2 h_2 j$ cross section by the purple dashed line for $\lambda_{345}^{\rm max}$ in Fig. 14 (left panel). One can see that 2.3 fb^{-1} monojet data are not quite sensitive even to the combined $h_1 h_1 j$ and $h_2 h_2 j$ signal at $\lambda_{345}^{\rm max}$.

As mentioned above, the $h_1 h_2 j$ production is mediated by Z-boson exchange (see Fig. 6) and has therefore a different $E_T^{\rm miss}$, so we investigate it separately. The right panel of Fig. 14 presents the limit for the $h_1 h_2 j$ production process (for $\Delta M = 1$ GeV) and indeed demonstrates that

the cross section limit for this process is different from the $h_1 h_1 j$ one because of their different kinematics. This process does not depend on the λ_{345} coupling, and thus the cross section is determined by the masses of h_1 and h_2; only, here, the expected signal rate represented by the red line indicates that it is well below the present limit.

3. Projections for the HL-LHC

For a next step in our study, we have found the projected LHC potential at higher integrated luminosities of 30, 300, and 3000 fb^{-1} with the last value posited as the ultimate benchmark for the HL-LHC. For this study, we made the following simplifying assumptions:

(i)   The SM background to the monojet searches at the HL-LHC is still going to be dominated by inclusive EW production of W and Z bosons, with strong production of $t\bar{t}$ pairs being a minor background.

(ii) The upgraded experiments will be successful in maintaining the physics performance demonstrated during Run 1 and Run 2, even in view of a much higher pileup in the range of $\langle PU \rangle = 140$–200.

(iii) The change from 13 to 14 TeV center-of-mass energy will not change the kinematic distribution of the reconstructed object in any significant way, neither for the SM background nor for the i2HDM processes.
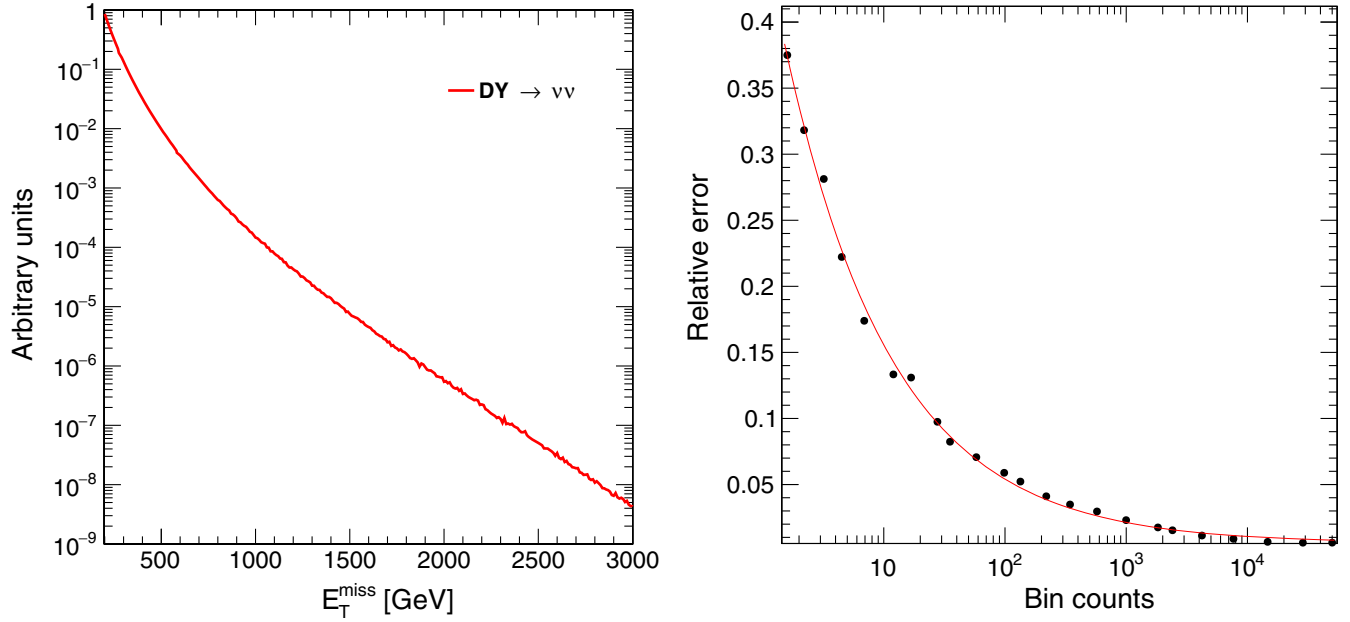
FIG. 15.   Left: E_T^{miss} distribution from $pp \to Z \to \nu\bar{\nu}j$ process produced with CALCHEP, for pp collisions at $\sqrt{s} = 13$ TeV. Right: Relative error in the background estimate as a function of bin counts, as extracted from Table III.

(iv) The overall analysis strategy will be kept very similar to that in Table II. As such, shape, yield, and uncertainty of both the signal and background can be scaled to the desired luminosities.

While the extrapolation of the signal distributions to the HL-LHC is a simple rescaling, the estimate of the tails of the W/Z inclusive p_T distributions is far from trivial. For the purposes of our study, we estimated the shape of the SM background directly from a simulation of $Z \to \nu\bar{\nu}j$ produced with CALCHEP, shown in the left panel of Fig. 15, while the normalization is approximated by a rescaling of the CMS results, since the efficiency of the selection is assumed to be the same. Since the background is primarily estimated from data distributions in control regions, we expect that the overall uncertainty in the E_T^{miss} prediction follows approximately a $1/\sqrt{N}$ distribution. The right panel of Fig. 15 shows the relative errors in each bin from Table III as a function of the bin content. One can see that, indeed, it follows the aforementioned distribution, but in addition, it also has a constant term ($\sim 0.6\%$) that can be understood to represent uncertainties that are not statistical in nature. We use the following equation for our bin-by-bin error estimate,

$$\sigma_{bin}^{(rel)} \equiv \frac{\sigma_{bin}}{N_{bin}} \simeq \frac{0.46}{\sqrt{N_{bin}}} + 0.6\%, \qquad (10)$$

where N_{bin} and σ_{bin} are the content and uncertainty of the given bin. The numerical values in Eq. (10) are obtained through a fit to the relative errors from Table III.

Our final background estimate for the extrapolation to the HL-LHC is therefore done through the following procedure:

(i) We find the shape of the E_T^{miss} distribution from the $pp \to Z \to \nu\bar{\nu}j$ process (Fig. 15).

(ii) We normalize the histogram such that the integral I_L in the range 200–1250 GeV is
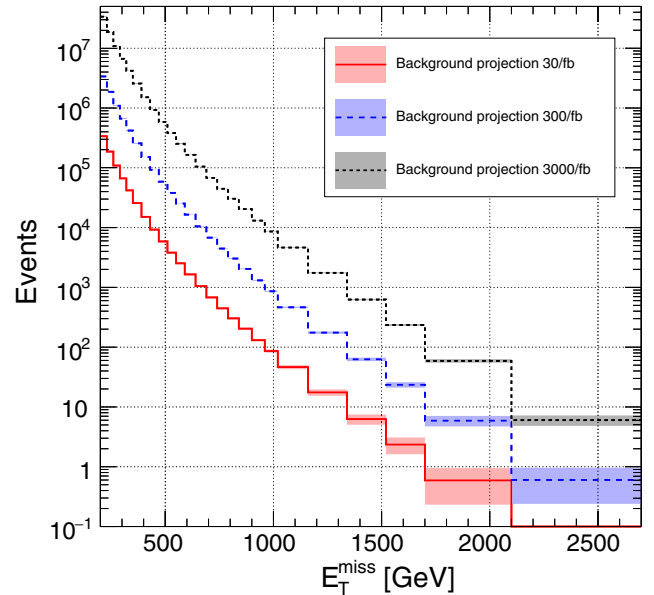

FIG. 16.   Background extrapolation for 30 (red solid line), 300 (blue dashed line), and 3000 fb^{-1} (black dotted line). The errors (shaded areas) are estimated through the procedure described in the text.
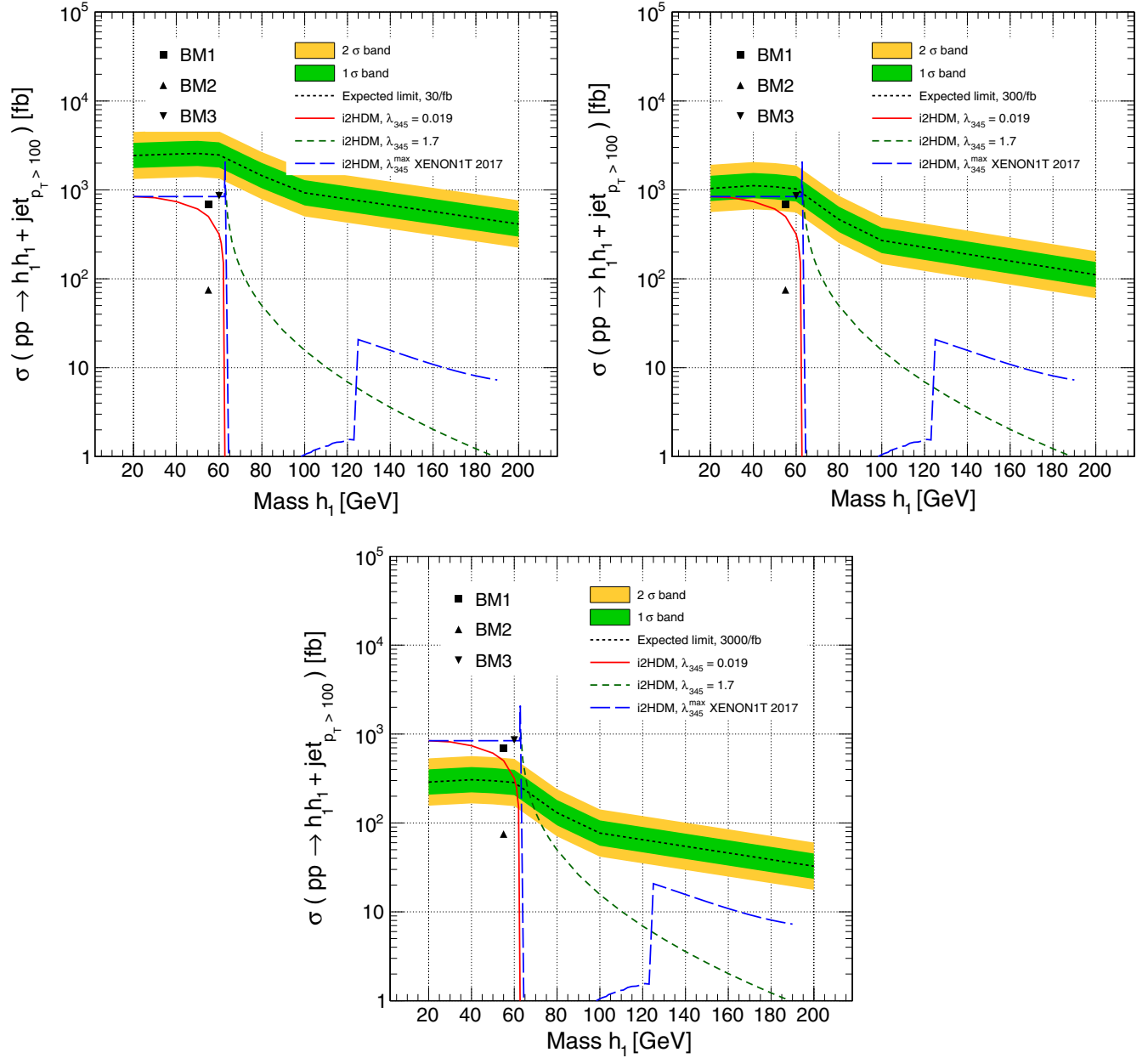
FIG. 17. Expected limits for the $h_1 h_1 j$ process for 30 (top left), 300 (top right), and 3000 fb^{-1} (bottom). The red solid line is the cross section for the parameter set $\lambda_{345} = 0.019$, $M_{h_2} = 200$ GeV, while the green short dashed line is the cross section for the parameter set $\lambda_{345} = 1.7$, $M_{h_2} = 200$ GeV. The blue dashed line is the combined contribution $h_1 h_1 j + h_1 h_2 j$ for $M_{h_2} = M_{h_1} + 1$ GeV and the maximal value of λ_{345}^{max} allowed by XENON1T data (see the text). The isolated symbols represent the benchmark points discussed in Table I. All cross sections are always given for a $p_T^{jet} > 100$ GeV requirement.

$$I_L = \frac{L_{\text{target}}}{L_{2015}} \cdot N_{\text{events}},$$

where L_{target} is the target luminosity (30, 300, or 3000 fb^{-1}), $L_{2015} = 2.3$ fb^{-1} is the integrated luminosity of Ref. [72], and $N_{\text{events}} = 61978.6$ is the total number of events in the aforementioned range, from Table III. This normalization is produced to

approximate the efficiency of the CMS selection on the real SM background.

(iii) We find the bin-by-bin errors according to the formula in Eq. (10).

This procedure guarantees that our background estimate has a reasonably correct shape, normalization, and uncertainty. Figure 16 shows the background extrapolation for 30, 300, and 3000 fb^{-1} together with the errors. The signal shapes are the same as in Fig. 12, and with these inputs, we

then evaluate the expected limits for the values of integrated luminosity under consideration.

In Fig. 17, we present the 95% CL limits for the $h_1 h_1 j$ and $h_2 h_2 j$ processes as function of M_{h_1}, together with production cross sections for $\lambda_{345} = 0.019$ (red solid line) and $\lambda_{345} = 1.7$ (green short dashed line) with $M_{h_2} = 200$ GeV, for both values of λ_{345}. The blue dashed line is the combined cross section for $h_1 h_1 j + h_1 h_2 j$ production for $M_{h_2} = M_{h_1} + 1$ GeV and the maximal value of $\lambda_{345}^{\max}$ allowed by XENON1T data. We find that,

with 30 fb^{-1} of integrated luminosity, one can exclude masses very close to $M_H/2$, for the maximum allowed value of λ_{345}. Further, with 3000 fb^{-1} of the HL-LHC, one will be able to exclude all the region of $M_{h_1} < M_H/2$ for $\lambda_{345} = 0.019$. At the same time, one can see that for values of λ_{345} allowed by XENON1T LHC it will not be possible to probe $M_{h_1} > M_H/2$ with 3000 fb^{-1} with $h_1 h_1 j / h_2 h_2 j$ process even if its cross section is maximized for $M_{h_1} \simeq M_{h_2}$. In Fig. 17, we also present the relevant benchmark points discussed in Table I. One can see that
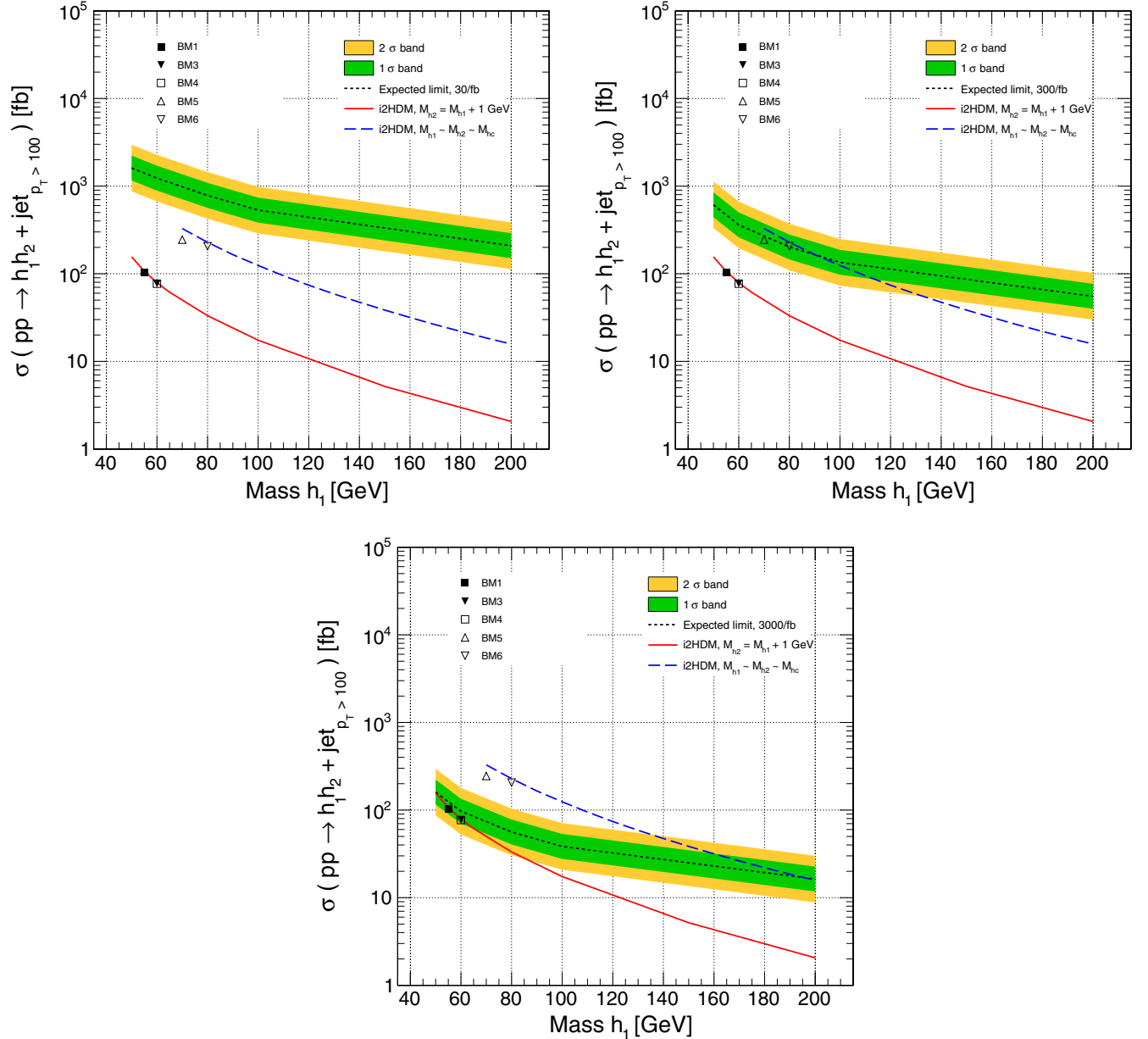

FIG. 18.   Expected limits for the $h_1 h_2 j$ process for 30 (top left), 300 (top right), and 3000 fb^{-1} (bottom). The red solid line is the cross section for $M_{h_2} = M_{h_1} + 1$ GeV. The blue short dashed line presents the cross section for the case when all inert scalars are close in mass: $M_{h_2} = M_{h_c} = M_{h_1} + 1$ GeV. The cross section is plotted for values of M_{h_1} larger than ~70 GeV, corresponding to the LEP bound for the charged Higgs [45]. The isolated symbols represent the benchmark points from Table I. All cross sections are always given for a $p_T^{\text{jet}} > 100$ GeV requirement.

BM1 and BM3 with large (but still experimentally allowed) Br($H \to h_2 h_2$) and Br($H \to h_1 h_1$), respectively, can be probed at the LHC at high luminosity. One should note that these benchmarks predict a too-low DM relic density, requiring additional source for DM from somewhere else. At the same time, the BM2 scenario with a DM relic density, which is in agreement with the upper and lower limits from Planck Collaboration, requires, respectively, too-low values of λ_{345} and too-low Br($H \to h_1 h_1$) = 0.022 to be observed at the LHC even in the high-luminosity stage. We would like to stress, however, that future DM DD experiments including XENON will be able to probe this benchmark since, as one can see from Table I, the σ_{SI}^p is already close to the XENON1T exclusion limit.

In Fig. 18, we present the 95% CL limits for the $h_1 h_2 j$ process as function of M_{h_1}. Only for very high luminosity and for lower $M_{h_1} \simeq M_{h_2}$ masses, the LHC might be sensitive to this process alone. It is important to stress once again that this process does not depend on λ_{345} and is therefore very complementary to the Higgs boson mediated one. One should notice that, in the $M_{h_1} \simeq M_{h_2}$ region, the actual limit should be given by a combination of this process with the $h_1 h_1 j$ and $h_2 h_2 j$ ones. The $h_1 h_1 j$ and $h_2 h_2 j$ combination is a trivial one; we just sum both cross sections, and the limit is given by Fig. 17. However, the combination with the $h_1 h_2 j$ process is not trivial since it has a different shape of E_T^{miss} distribution and the relative weights of $h_1 h_1 j/h_2 h_2 j$ and $h_1 h_2 j$ distributions are eventually dependent on the value of λ_{345}. One should also note that the sensitivity of the LHC to the $h_1 h_1 j/h_2 h_2 j$ process is very limited for $M_{h_1} > M_H/2$ as one can see from Fig. 17 since XENON1T puts a very stringent upper limit on the λ_{345} coupling. Therefore, the $h_1 h_2 j$ process is likely to be a unique one for the LHC to probe the i2HDM parameter space beyond for $M_{h_1} > M_H/2$. If all (pseudo)scalar masses, M_{h_1}, M_{h_2}, and M_{h^+}, are similar, the LHC will be sensitive to the M_{h_1} up to about 100 GeV with 300 fb^{-1} and up to about 200 GeV with 3000 fb^{-1} as demonstrated in the right and bottom frames of Fig. 18, respectively. The red solid line in this figure gives the cross section for $M_{h_2} = M_{h_1} + 1$ GeV, while the blue short dashed line is the cross section for the case when all inert scalars are close in mass ($M_{h_2} = M_{h_c} = M_{h_1} + 1$ GeV) and the processes with the charged scalar(s) mimics the signature from the $h_1 h_2 j$ process. Figure 18 shows that benchmarks BM5 and BM6 with all nearly degenerate inert scalars can be tested already with 300 fb^{-1} integrated luminosity, while BM1, BM3, and BM4 with nearly degenerate h_1 and h_2 can be excluded with 3000 fb^{-1}.

One can finally use the dependence of the cross section upon λ_{345} to calculate an exclusion region on the (M_{h_1}, λ_{345}) plane. Figure 19 shows the excluded values of λ_{345} as function of M_{h_1} for 3000 fb^{-1}. A monojet search at the HL-LHC will therefore exclude values of λ_{345} larger than
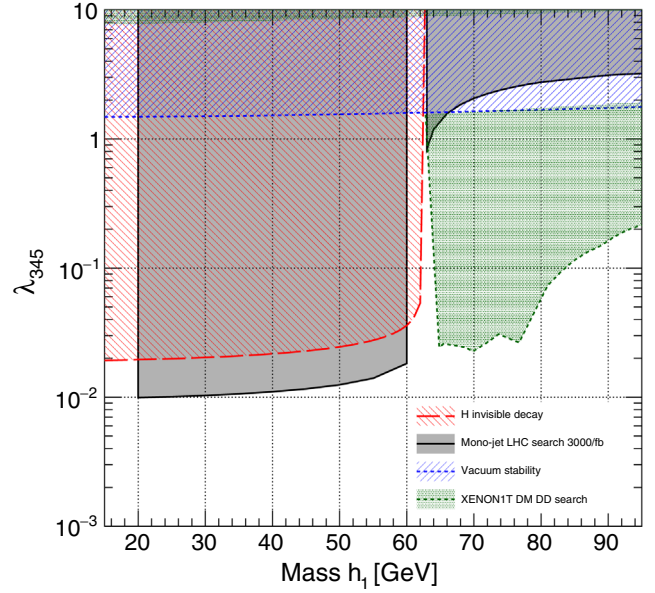

FIG. 19. Expected exclusion region on the (M_{h_1}, λ_{345}) plane for 3000 fb^{-1}. The curve corresponding to Eq. (7) is given by the red dashed contor, while the expected result for 3000 fb^{-1} is given by the black solid contour. Also shown are the limits from vacuum stability (hashed blue region, dotted contour) and the XENON1T direct detection search (shaded green region, dotted contour).

0.011–0.02, for the range of masses $M_{h_1} < M_H/2$. For higher values of M_{h_1}, one would instead need a coupling value as large as $\lambda_{345} = 4.9$ in order to exclude $M_{h_1} < 100$ GeV. Also shown are the experimentally excluded regions from the invisible Higgs decay constraints as well the theoretically allowed maximum of λ_{345} from vacuum stability.

IV. CONCLUSIONS

In this paper, we have assessed the scope of the LHC in accessing a monojet signal stemming from the i2HDM wherein the lightest inert Higgs state h_1 is a DM candidate, produced in pairs from gluon-gluon fusion into the SM-like Higgs H and accompanied by (at least) a hard jet with transverse momentum above 100 GeV, i.e., a $h_1 h_1 j$ final state. The second-lightest inert Higgs boson h_2 can also contribute to a monojet signature, whenever it is degenerate enough with the lightest one so that its decay products produced alongside the h_1 state are too soft to be detected. This can happen in $h_2 h_2 j$ (again produced by gluon-gluon fusion into the SM-like Higgs) as well as $h_1 h_2 j$ (induced by Z mediation) final states.

Before proceeding to such an assessment, we have established the viable parameter space of the i2HDM following both theoretical and experimental constraints. The former are dominated by vacuum stability requirements, whereas the latter are extracted from LEP, EWPT, LHC, relic density, as well as LUX and, especially,

XENON1T data, which greatly reduce the accessible volume of i2HDM parameter space. The established impact of XENON1T results is in fact one of the main results of our analysis.

Over the surviving i2HDM parameter space, we have defined several benchmark points, wherein M_{h_1} varies from 55 to 80 GeV and M_{h_2} is between 1 and 55 GeV apart, and tested them against a CMS inspired selection. However, in relation to the latter, we have adopted a somewhat orthogonal approach, as we have exploited the shape of the E_T^{miss} distribution (as opposed to a standard counting experiment analysis). We have indeed shown that the shape analysis is able to obtain a better sensitivity than a counting experiment. Furthermore, we have extrapolated such sensitivity to much higher luminosities, typical of the end of the Run 2, Run 3, and high-luminosity LHC.

By adopting an improved version of standard analysis tools (i.e., matrix element, parton shower, and hadronization generators as well as detector software), which further accounts for a k-factor enabling us to correct the EFT approach for the emulation of the explicit loop entering the $gg \to H$ process in the signal and a sophisticated background treatment, we have been able to establish that the advocated shape analysis has significant scope in constraining monojet signals induced by i2HDM dynamics.

We have found that $h_1 h_1 j$ (plus $h_2 h_2 j$) and $h_1 h_2 j$ processes are very complementary to each other in probing the i2HDM parameter space. The former covers the $M_{h_1} < M_H/2$ region and will allow us to put constraints on (in the case of void searches) or else extract (in the case of discovery) two fundamental parameters of the i2HDM entering the leading monojet process. These are the h_1 mass and the trilinear self-coupling λ_{345} connecting the SM-like Higgs to the DM candidate pair. For example, for $M_{h_1} < M_H/2$, no values for λ_{345} above 0.01–0.03 would be allowed in the case of no discovery. At the same time, this process is not sensitive to $M_{h_1} > M_H/2$ for values of λ_{345}

allowed by DM DD constraints. On the other hand, λ_{345}-independent $h_1 h_2 j$ process can be used to probe the $M_{h_1} > M_H/2$ region of the parameter space via monojet signature in case $M_{h_1} \simeq M_{h_2}$. Moreover, the $h_1 h_2 j$ process has a slightly less steeply falling E_T^{miss} distribution than the $h_1 h_1 j$ one because of different mediator (Z boson instead of Higgs boson) and, consequently, a slightly better LHC limit. If all the (pseudo)scalar masses, M_{h_1}, M_{h_2}, and M_{h^+}, are similar, the LHC will be sensitive to M_{h_1} up to about 100 GeV with 300 fb^{-1} and up to about 200 GeV with 3000 fb^{-1}.

[1] P. J. Fox, R. Harnik, J. Kopp, and Y. Tsai, Phys. Rev. D **85,** 056011 (2012).

[2] A. Rajaraman, W. Shepherd, T. M. P. Tait, and A. M. Wijangco, Phys. Rev. D **84,** 095013 (2011).

[3] J. Goodman, M. Ibe, A. Rajaraman, W. Shepherd, T. M. Tait, and H.-B. Yu, Phys. Rev. D **82,** 116010 (2010).

[4] Y. Bai, P. J. Fox, and R. Harnik, J. High Energy Phys. 12 (2010) 048.

[5] M. Beltran, D. Hooper, E. W. Kolb, Z. A. C. Krusberg, and T. M. P. Tait, J. High Energy Phys. 09 (2010) 037.

[6] J. Goodman, M. Ibe, A. Rajaraman, W. Shepherd, T. M. P. Tait, and H.-B. Yu, Phys. Lett. B **695,** 185 (2011).

[7] P. J. Fox, R. Harnik, J. Kopp, and Y. Tsai, Phys. Rev. D **84,** 014028 (2011).

[8] I. M. Shoemaker and L. Vecchi, Phys. Rev. D **86,** 015023 (2012).

[9] P. J. Fox and C. Williams, Phys. Rev. D **87,** 054030 (2013).

[10] U. Haisch, F. Kahlhoefer, and J. Unwin, J. High Energy Phys. 07 (2013) 125.

[11] G. Busoni, A. De Simone, E. Morgante, and A. Riotto, Phys. Lett. B **728,** 412 (2014).

[12] G. Busoni, A. De Simone, J. Gramling, E. Morgante, and A. Riotto, J. Cosmol. Astropart. Phys. 06 (2014) 060.

[13] A. Belyaev, L. Panizzi, A. Pukhov, and M. Thomas, J. High Energy Phys. 04 (2017) 110.

[14] O. Buchmueller, M. J. Dolan, and C. McCabe, J High. Energy Phys. 01 (**2014**) 025.

[15] G. Busoni, A. De Simone, J. Gramling, E. Morgante, and A. Riotto, J. Cosmol. Astropart. Phys. 06 (2014) 060.

[16] G. Busoni, A. De Simone, T. Jacques, E. Morgante, and A. Riotto, J. Cosmol. Astropart. Phys. 09 (2014) 022.

[17] O. Buchmueller, M. J. Dolan, S. A. Malik, and C. McCabe, J High. Energy Phys. 01 (**2015**) 037.

[18] M. R. Buckley, D. Feld, and D. Goncalves, Phys. Rev. D **91,** 015017 (2015).

[19] J. Abdallah et al., Phys. Dark Universe **9–10,** 8 (2015).

[20] J. Abdallah, A. Ashkenazi, A. Boveia, G. Busoni, A. De Simone et al., arXiv:1409.2893.

[21] D. Abercrombie et al., arXiv:1507.00966.

[22] N. G. Deshpande and E. Ma, Phys. Rev. D **18,** 2574 (1978).

[23] E. Ma, Phys. Rev. D **73,** 077301 (2006).

[24] R. Barbieri, L. J. Hall, and V. S. Rychkov, Phys. Rev. D **74,** 015007 (2006).

[25] L. Lopez Honorez, E. Nezri, J. F. Oliver, and M. H. Tytgat, J. Cosmol. Astropart. Phys. 02 (2007) 028.

[26] C. Arina, F.-S. Ling, and M. H. G. Tytgat, J. Cosmol. Astropart. Phys. 10 (2009) 018.

[27] E. Nezri, M. H. G. Tytgat, and G. Vertongen, J. Cosmol. Astropart. Phys. 04 (2009) 014.

[28] X. Miao, S. Su, and B. Thomas, Phys. Rev. D **82,** 035009 (2010).

[29] M. Gustafsson, S. Rydbeck, L. Lopez-Honorez, and E. Lundstrom, Phys. Rev. D **86,** 075019 (2012).

[30] A. Arhrib, R. Benbrik, and N. Gaur, Phys. Rev. D **85,** 095021 (2012).

[31] B. Swiezewska and M. Krawczyk, Phys. Rev. D **88,** 035019 (2013).

[32] A. Goudelis, B. Herrmann, and O. Stål, J. High Energy Phys. 09 (2013) 106.

[33] A. Arhrib, Y.-L. S. Tsai, Q. Yuan, and T.-C. Yuan, J. Cosmol. Astropart. Phys. 06 (2014) 030.

[34] M. Krawczyk, D. Sokolowska, P. Swaczyna, and B. Swiezewska, J. High Energy Phys. 09 (2013) 055.

[35] M. Krawczyk, D. Sokołowska, P. Swaczyna, and B. Świeżewska, Acta Phys. Pol. B **44,** 2163 (2013).

[36] A. Ilnicka, M. Krawczyk, and T. Robens, Phys. Rev. D **93,** 055026 (2016).

[37] M. A. Díaz, B. Koch, and S. Urrutia-Quiroga, Adv. High Energy Phys. **2016,** 8278375 (2016).

[38] K. P. Modak and D. Majumdar, Astrophys. J. Suppl. Ser. **219,** 37 (2015).

[39] F. S. Queiroz and C. E. Yaguna, J. Cosmol. Astropart. Phys. 02 (2016) 038.

[40] C. Garcia-Cely, M. Gustafsson, and A. Ibarra, J. Cosmol. Astropart. Phys. 02 (2016) 043.

[41] M. Hashemi and S. Najjari, Eur. Phys. J. C **77,** 592 (2017).

[42] P. Poulose, S. Sahoo, and K. Sridhar, Phys. Lett. B **765,** 300 (2017).

[43] A. Alves, D. A. Camargo, A. G. Dias, R. Longas, C. C. Nishi, and F. S. Queiroz, J. High Energy Phys. 10 (2016) 015.

[44] A. Datta, N. Ganguly, N. Khan, and S. Rakshit, Phys. Rev. D **95,** 015017 (2017).

[45] A. Belyaev, G. Cacciapaglia, I. P. Ivanov, F. Rojas-Abatte, and M. Thomas, Phys. Rev. D **97,** 035011 (2018).

[46] G. Aad et al. (ATLAS Collaboration), J. High Energy Phys. 01 (2016) 172.

[47] V. Khachatryan et al. (CMS Collaboration), J. High Energy Phys. 02 (2017) 135.

[48] A. Belyaev, N. D. Christensen, and A. Pukhov, Comput. Phys. Commun. **184,** 1729 (2013).

[49] G. Belanger, F. Boudjema, A. Pukhov, and A. Semenov, Comput. Phys. Commun. **149,** 103 (2002).

[50] G. Belanger, F. Boudjema, A. Pukhov, and A. Semenov, Comput. Phys. Commun. **174,** 577 (2006).

[51] P. A. R. Ade et al. (Planck Collaboration), Astron. Astrophys. **571,** A16 (2014).

[52] P. A. R. Ade et al. (Planck Collaboration), Astron. Astrophys. **594,** A13 (2016).

[53] D. S. Akerib et al. (LUX Collaboration), Phys. Rev. Lett. **112,** 091303 (2014).

[54] E. Aprile et al. (XENON Collaboration), Phys. Rev. Lett. **119,** 181301 (2017).

[55] Digitized XENON1T results at PhenoData project, https://hepmdb.soton.ac.uk/phenodata/view.php?id=595e239abb817586383e929d.

[56] A. Ilnicka, T. Robens, and T. Stefaniak, Mod. Phys. Lett. A **33,** 1830007 (2018).

[57] M. Bondarenko, A. Belyaev, J. Blandford, L. Basso, E. Boos, V. Bunichev et al., arXiv:1203.1488.

[58] R. D. Ball et al., Nucl. Phys. **B867,** 244 (2013).

[59] D. de Florian et al. (LHC Higgs Cross Section Working Group), arXiv:1610.07922.

[60] J. Alwall, M. Herquet, F. Maltoni, O. Mattelaer, and T. Stelzer, J. High Energy Phys. 06 (2011) 128.

[61] J. Alwall, R. Frederix, S. Frixione, V. Hirschi, F. Maltoni, O. Mattelaer, H. S. Shao, T. Stelzer, P. Torrielli, and M. Zaro, J. High Energy Phys. 07 (2014) 079.

[62] J. M. Lindert, K. Kudashkin, K. Melnikov, and C. Wever, Phys. Lett. B **782,** 210 (2018).

[63] S. P. Jones, M. Kerner, and G. Luisoni, Phys. Rev. Lett. **120,** 162001 (2018).

[64] T. Neumann, J. Phys. Commun. **2,** 095017 (2018).

[65] T. Sjostrand, S. Mrenna, and P. Z. Skands, J. High Energy Phys. 05 (2006) 026.

[66] T. Sjostrand, S. Mrenna, and P. Z. Skands, Comput. Phys. Commun. **178,** 852 (2008).

[67] A. Buckley, J. Ferrando, S. Lloyd, K. Nordström, B. Page, M. Rüfenacht, M. Schönherr, and G. Watt, Eur. Phys. J. C **75,** 132 (2015).

[68] J. de Favereau, C. Delaere, P. Demin, A. Giammanco, V. Lemaître, A. Mertens, and M. Selvaggi (DELPHES 3 Collaboration), J. High Energy Phys. 02 (2014) 057.

[69] A. L. Read, J. Phys. G **28,** 2693 (2002).

[70] G. Cowan, K. Cranmer, E. Gross, and O. Vitells, Eur. Phys. J. C **71,** 1554 (2011); **73,** 2501(E) (2013).

[71] T. Müller, J. Ott, and J. Wagner-Kuhr, http://www-ekp.physik.uni-karlsruhe.de/~ott/theta/theta-auto/index.html.

[72] (CMS Collaboration) Report No. CMS-PAS-EXO-16-013, 2016.

[73] V. Khachatryan et al. (CMS Collaboration), Eur. Phys. J. C **75,** 235 (2015).